The Pennsylvania State University

The Graduate School

Department of Materials Science and Engineering

EVALUATING SOURCES AND ROOT CAUSES OF PORE FORMATION IN ELECTRON

BEAM-BASED DIRECTED ENERGY DEPOSITION OF TITANIUM COMPONENTS

A Thesis in

Materials Science and Engineering

by

Kyle R. Snyder

Submitted in Partial Fulfillment
of the Requirements
for the Degree of

Master of Science

August 2018

The thesis of Kyle R. Snyder was reviewed and approved* by the following:

Richard Martukanitz
Thesis Advisor

Allison Beese
Assistant Professor of Materials Science and Engineering

Todd Palmer
Professor of Materials Science and Engineering

Edward Reutzel
Professor of Engineering Science and Mechanics

Suzanne Mohney
Professor of Materials Science and Engineering
Chair, Intercollege Graduate Degree Program in Materials Science and Engineering

*Signatures are on file in the Graduate School.

ABSTRACT

Porosity is a common issue in additive manufacturing of titanium and its alloys, causing detrimental effects on mechanical properties and limiting potential applications for high performance components. The goal of this project was to establish sources and root causes of pore formation in electron beam processing and determine their influence on porosity. Potential sources were identified as, porosity from hydrogen evolution, aluminum vaporization, and melt pool lifetime. A factorial experiment was designed to evaluate the effects of hydrogen evolution through filler wire quality and the effects of aluminum vaporization by varying the aluminum content in the filler wire by using Ti-6Al-4V (Ti-64) and CP-Ti alloys in an electron beam-based directed energy deposition process.

Several characterization techniques were implemented to determine the total degree of porosity for each run condition. Analysis of the raw data as well as statistical approaches were applied to improve the interpretation of the response variable (porosity) in terms of the independent variables. An analysis of variance (ANOVA) was conducted using different pore characteristics as responses for different variables, aside from the selected experimental variables.

Next, a theoretical model for pore formation was developed to create a physical understanding of the experimental results. Three main mechanisms for pore formation were identified and used as the basis for this this model. The formation mechanisms depend on several factors including the amount of time available for each mechanism to act, temperature of process, and properties of the liquid metal. Time and temperature of the process are considered to be consistent for all samples, but the addition of

alloying elements alters the properties of liquid titanium meaning Ti-6Al-4V will have different liquid

properties than CP-Ti. Alloying titanium with aluminum alters the liquid metal properties of titanium to

favor an increase in the degree of porosity based on the classical pore formation mechanisms.

TABLE OF CONTENTS

LIST OF FIGURES

LIST OF TABLES

ACKNOWLEDGEMENTS

Chapter 1: Introduction

Additive manufacturing (AM) is a rapidly growing field that is applied to various applications related to automotive, aerospace, and medical industries [1]. As technology in AM improves, the range of applications continues to expand, but with limitations. Since AM is a relatively new process, there is still a lack of understanding throughout many aspects of the process. Also, due to a lack of standards, it is difficult to verify the quality of parts that are produced. Discrepancies in part quality may include dimensional precision and tolerances, internal and external defects, and undesirable microstructures due to complex thermal histories [1,2].

Porosity is seen in all AM processes, but micro-porosity is a common and unexplained phenomenon in electron beam-based directed energy deposition (EB-DED) [1,3]. Due to the detrimental effects porosity has on mechanical properties, this becomes an issue for components that require a high level of performance for their application. If AM is expected to continue growing, a better understanding of the process must be developed in order to minimize negative effects such as porosity [1].

Titanium alloy Ti-6Al-4V (Ti-64) is a commonly used material in all metal additive manufacturing processes. It is an attractive alloy due to its high strength, low density, high melting temperature, and excellent corrosion resistance. These properties make Ti-6Al-4V ideal for several applications such as structural components in aerospace, automotive, and chemical industries [1,2].

The goal of this project was to establish source(s) and root cause(s) of pore formation during electron beam-based directed energy deposition. This was done by first conducting and extensive literature review to determine possible sources and causes of porosity. Once these were identified, a design of experiment was created to test the potential sources and causes that were expected to have the greatest

impact on porosity. After experimentation, optical microscopy (OM), scanning electron microscopy

(SEM), and x-ray computed tomography (x-ray CT) were used to evaluate size, location and morphology

of pores. Stereology and analysis of variance (ANOVA) statistical methods were applied to improve the

understanding between pore characteristics and the experimental independent variables. Finally, a

theoretical model for pore formation was developed and used to compare to the results from OM, SEM,

and X-ray CT.

Chapter 2: Literature Review and Experimental Background

Additive Manufacturing

Additive Manufacturing (AM), as defined by ASTM International, is a process of joining materials to make objects from 3D model data, usually layer upon layer, as opposed to subtractive methodologies [4]. Additionally, as AM technology developed, more new systems were developed, causing confusion when communicating information for education or development purposes. To simplify, ASTM International separated the processes into seven categories, combining systems with similar processing methods to create a standard terminology for AM process categories [4]. The categories are listed in Table 1 along with additional information including common materials used, process specifications, applications, and other important information [1-4].

Metal AM

Metal AM capabilities have been developed to offer promising manufacturing technology to produce parts with improved performance over other traditional manufacturing methods [1,2]. As you can see from Table 1, AM of metal components can be done using DED, material extrusion, PBF, or sheet lamination process methods, although DED and PBF are most commonly used and studied. Both DED and PBF processes use either a laser or electron beam (or possibly and less common, a plasma arc) as their energy source.

AM may offer several benefits over traditional manufacturing techniques, but still has many barriers to overcome before it can be considered a feasible processing method [1,3]. These barriers

include, but are not limited to, high costs of materials and processing, lack of process knowledge and

understanding, and limits in available materials and characterization capabilities [1-4]. Given all the

possible alloy combinations, only a small fraction of these metals can be processed using AM [1].

Common metals used in metal AM include titanium alloys, aluminum alloys, stainless steels, and nickel

superalloys [1,2].

Table 1: Table of AM process categories [1-4]			
Process Category	**Material Systems**	**Energy Source**	**Process Strengths and Weaknesses**
Binder Jetting	Polymer, metal, or ceramic powder	Thermal Energy	Wide range for material selection Implement full color prints High porosities- requires infiltration
Directed Energy Deposition (DED)	Metal powder	Laser or e- Beam	Requires post process machining Functionally graded materials Repair damaged parts
Material Extrusion	Thermalplastics, ceramic slurries, or metal paste	Thermal Energy	Low cost for machine Multi-material capabilities Low resolution and poor surface finish
Material Jetting	Photopolymer or wax	Thermal Energy	Multi-material printing Low-strength in final part High surface finish
Powder Bed Fusion (PBF)	Polymer or metal powder	Laser or e- Beam	High resolution, strength, and stiffness Fully dense parts Support and anchor structures
Sheet Lamination	Plastic film or metal sheet	Laser Beam	Low cost for machine, materials and process High surface finish
Vat Polymerization	Photopolymer or ceramic	UV Laser	Rapid build rate High cost of materials Good part resolution

Electron Beam Directed Energy Deposition

An electron beam is formed by passing a current through a filament to generate electrons. Once the

electrons are ejected from the filament, electrostatic forces accelerate them to 50% - 80% of the speed of

light. Due to the nature of electrons, charged particles with extremely low mass, they can be easily

manipulated by electrostatic lenses and focused into a beam. The beam can be further influenced to form

various raster patterns at oscillations up to 200 kHz, although 500Hz-2 kHz is a commonly used range.

The layout for generating and manipulating an electron beam is shown in Figure 1. To prevent scattering

from collisions with gas molecules, the electron beam is generated in a vacuum environment [3,5].
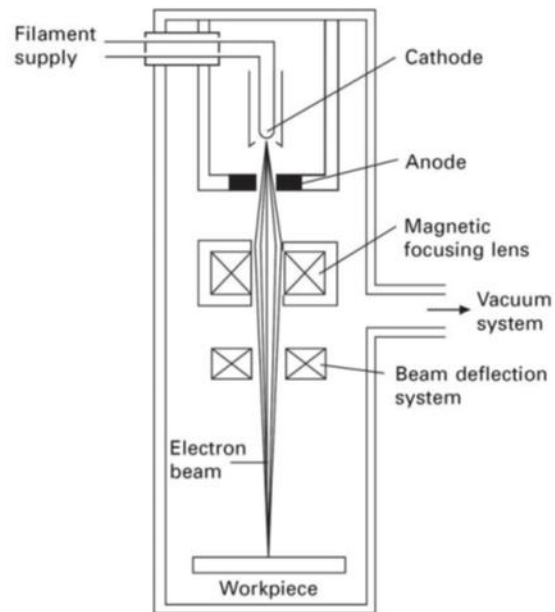
Figure 1: Schematic of electron beam process chamber reproduced from [5]

As the high velocity electrons hit the metal surface, they are rapidly decelerated and their kinetic energy is converted into thermal energy. The electron beam has a high energy density due to the high efficiency of the energy transformation process. The high energy input allows for higher deposition rates compared to lower energy laser processing. This leads to issues with vaporization and evaporation losses of materials with low vapor pressures. The vaporization issue is addressed by generating a raster pattern, which essentially defocuses the beam and decreases the energy density. Since the electrons are easily controlled through the electrostatic lenses, nearly any raster pattern can be generated. Common raster patterns can be seen in Figure 2 and include a circle, figure eight, and arrowhead [3,5]. Due to the simplicity of a circle in terms of generation and calculating energy density, raster pattern B from Figure 2, is most commonly used [3].
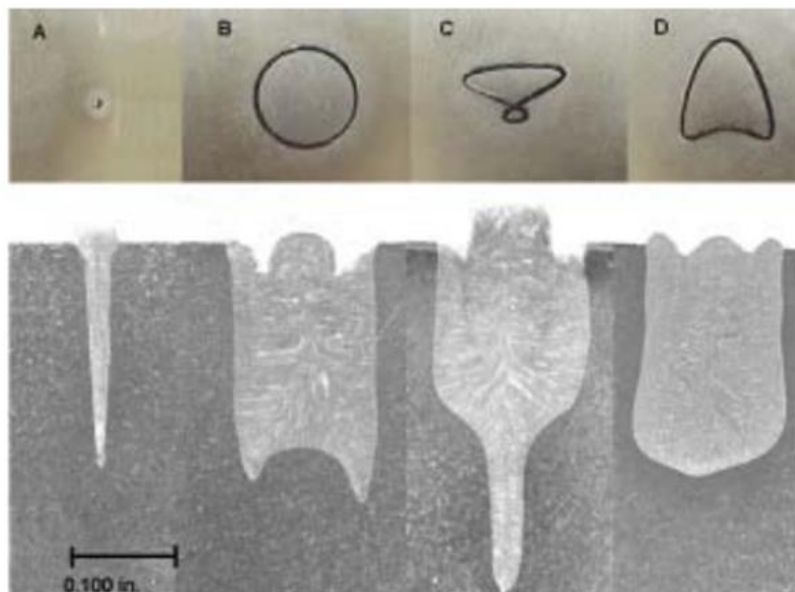
Figure 2: Common electron beam raster patterns and penetration profiles reproduced from [3]

Titanium and its Alloys

Metals like titanium, are of the exothermic occluding type and characteristically form hydrides when the total amount of hydrogen in the system exceeds the solubility limit of the material. Initially, hydrogen entering the system will be absorbed in solid-solution, leaving a single-phase metal. The level of hydrogen content at the onset of hydride formation is taken as the solubility limit of the metal. This is where the system departs from a single phase, solid-solution state and becomes a two-phase alloy including a hydride phase [7,8]. Figure 3 shows the three different phases (alpha, beta, and gamma) in the titanium-hydrogen equilibrium phase diagram at standard pressure [9]. Alpha phase has a maximum hydrogen solubility of 7.9 atomic percent at the eutectoid temperature of 319˚C. The maximum hydrogen solubility in the beta phase is 49 atomic percent and occurs at 640˚C. Finally, the gamma phase, or hydride phase, exists over the $TiH – TiH_2$ region of the phase diagram [7-9].

The differences in solubility limits between alpha and beta phase can be attributed to their different crystal structures. Hydrogen can exist in the system as a proton or as an atom, with a radius of 0.41Å, located in an interstitial site. Alpha phase has a hexagonal closed packed (HCP) crystal structure with two interstitial sites, tetrahedral and octahedral, as seen in Figure 4a and 4b. The tetrahedral and octahedral interstices can accommodate atoms with radii of 0.315Å and 0.59Å, respectively. This indicates that a majority of interstitial hydrogen atoms in alpha titanium occupy the larger octahedral sites, since they are unlikely to fit into the smaller tetrahedral interstices. Beta phase has a body centered cubic (BCC) crystal structure with a tetrahedral interstice, Figure 4c. The beta phase tetrahedral interstice can hold an atom with a radius of 0.44Å, slightly larger than the radius of a hydrogen atom. The close

match in size between the interstice site and hydrogen atom radius explains the higher hydrogen solubility in the beta phase compared to alpha phase [6].

Figure 5 shows the effect of the equilibrium hydrogen pressure on its solubility in titanium at various temperatures [9]. This indicates an increase in hydrogen solubility with increasing equilibrium pressure, most noticeable in the beta phase. Additionally, as the equilibrium pressure surrounding the titanium increases, the hydrogen concentration in the metal increases as well.

The solubility of hydrogen in Ti-6Al-4V will differ from CP-Ti due to different amounts of phases present [7-9]. As previously mentioned, beta phase has a higher hydrogen solubility than alpha phase, so increasing the amount of beta phase present will increase the solubility. Alloying with beta stabilizers, such as Mo, Cr, V, Mn, and Fe, will lower the beta transus, increase the amount of beta phase present and therefore increase the overall hydrogen solubility compared to unalloyed titanium. Additions of molybdenum have a greater effect on hydrogen solubility compared to alloying with other beta stabilizers. Additions of alpha stabilizers, such as Al, Zr, and Sn, increase the stability of the alpha phase. Aluminum is most commonly used in titanium alloys and is found to have a significant effect on the solubility of hydrogen in titanium. At low temperatures, aluminum additions increase hydrogen solubility, but at high temperatures, aluminum additions decrease hydrogen solubility. Aluminum additions strain the HCP lattice of titanium, decreasing the 'a' and 'c' lattice parameters as well as the size of the octahedral interstice in the alpha phase. The decreasing size of the octahedral interstice creates a better fit for a hydrogen atom and is most likely the reason for the increase in hydrogen solubility with the addition of aluminum at low temperatures. Paton et al. noticed that hydride nucleation was difficult in samples with higher aluminum contents and concluded that aluminum additions suppress hydride

formation [6]. This agrees with the increase in hydrogen solubility at low temperatures with the addition

of aluminum. As aluminum is added, the hydrogen solubility limit will increase, leaving less

supersaturated hydrogen available for hydride formation.
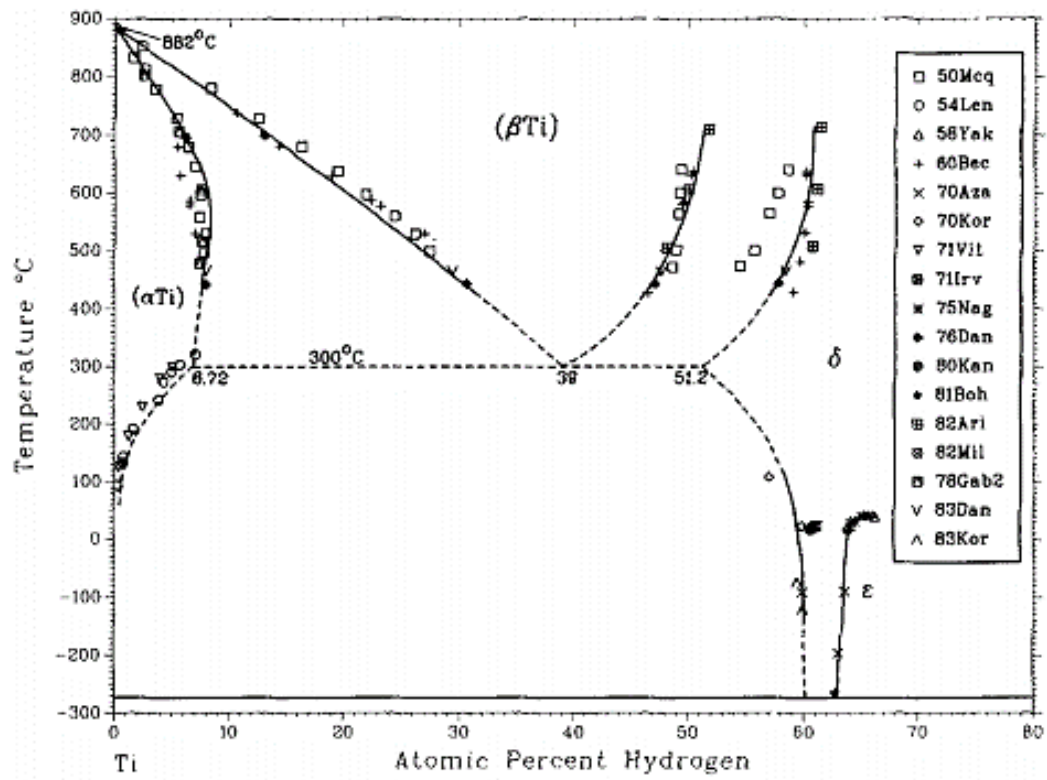
Figure 3: H-Ti phase diagram reproduced from [7]

a)
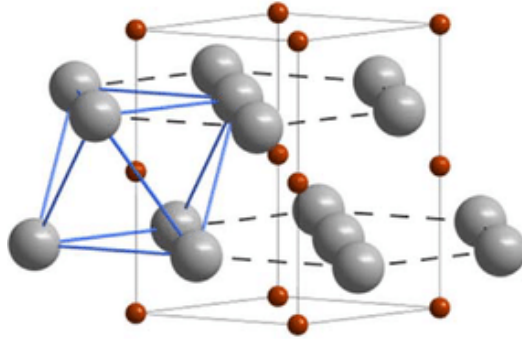
b)
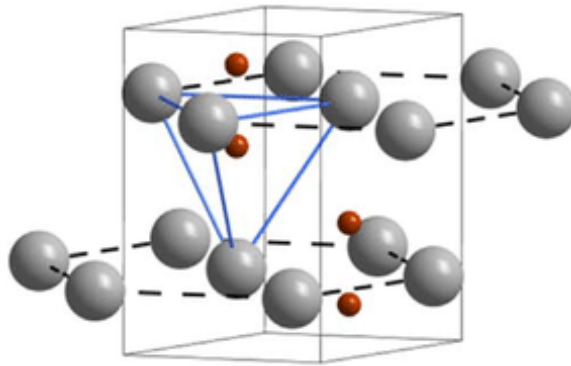
c)
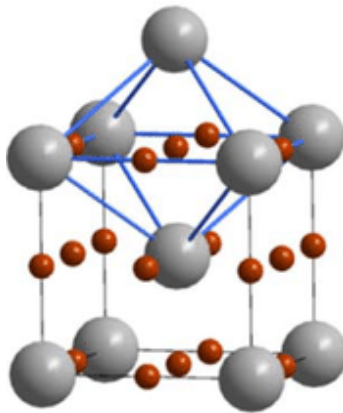
Figure 4: Crystal structure (gray) and interstices (orange) for HCP octahedral interstice (a), HCP tetrahedral interstice (b), and BCC octahedral interstice (c) reproduced from [7].
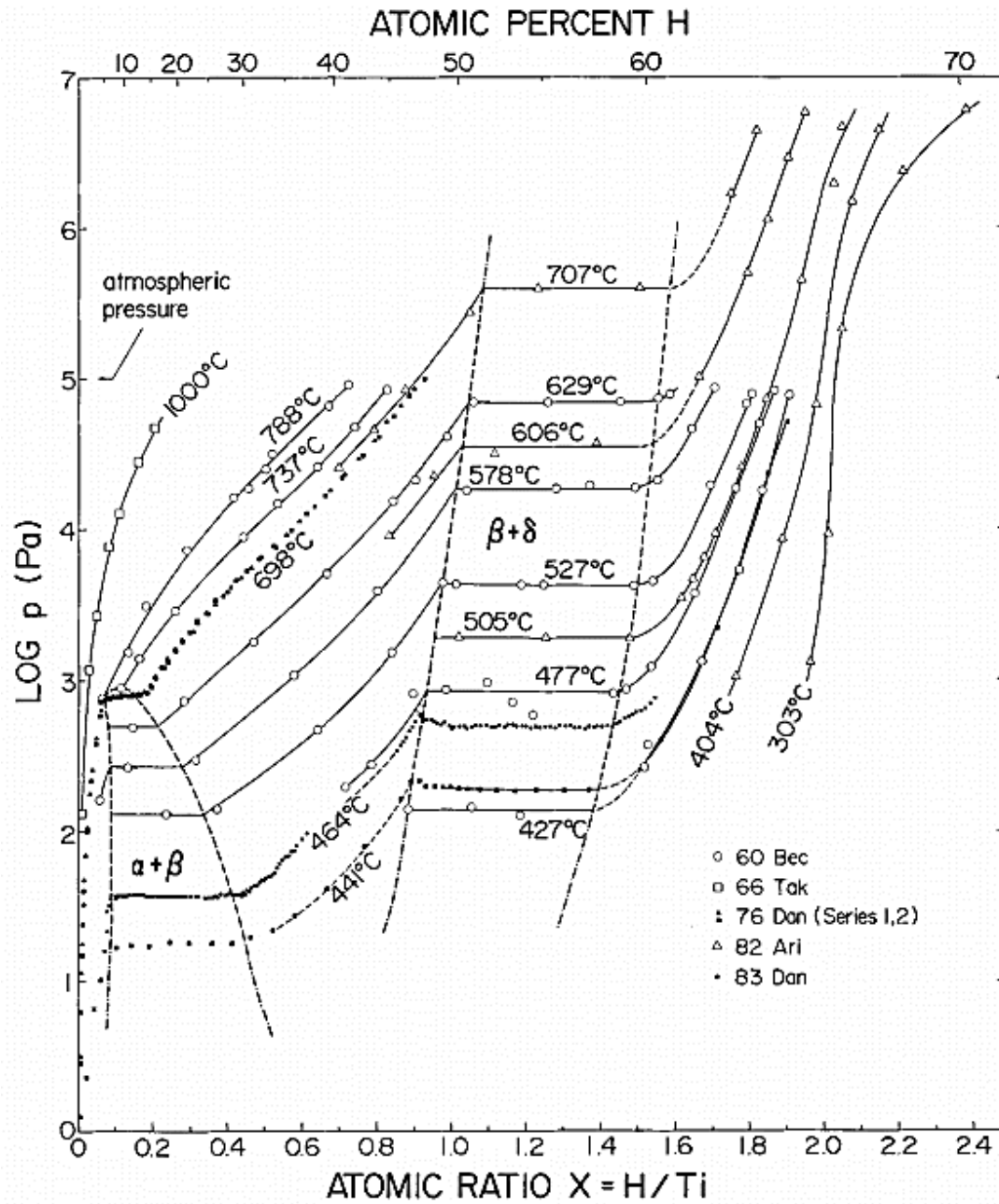
Figure 5: Effect of hydrogen partial pressure on hydrogen solubility reproduced by [7]

Wire Contamination

A previous experiment by Martukanitz et al. investigated sources of porosity in gas metal arc welding of aluminum, and the physical components of the system were evaluated. The results from this study showed that the largest influence on porosity came from the filler material that was used [10]. In another experiment, from the Applied Research Laboratory, four different wires were evaluated for quality based on the amounts of porosity produced. It was found that each of the four wires that were evaluated generated different amounts of porosity, indicating that there may be a difference in wire quality between different manufacturers [11]. The contamination of the wire could stem from two potential sources, impurities on the surface of the wire or impurities within the bulk of the wire. No initial analysis was reported for either experiment, so there is no way of determining whether the porosity was formed from contaminants on the surface of the wire, from bulk of the wire, or both [10,11]

Molybdenum disulfide (MoS$_2$) is used as a dry lubricant on the wire during the drawing process. Previous experiments have investigated the effects of interstitial element contamination in dry lubricants [12,13]. In these reports, SEM data showed the presence of contaminants in the materials processed with dry lubricants [12]. Molybdenum has a high polarization influence on easily polarized sulfur atoms, which causes the sulfur atoms to form dipoles. As MoS$_2$ crystallizes, a layered structure is formed with weak bonds between the strongly bonded layers. Layered structures with weak bonding forces is a characteristic of all dry lubricants. The lubricating mechanism comes from the small shear forces required to break the weak bonds between the layers of the structure. Figure 6 is a representation of the layer crystal structure that is formed from molybdenum and sulfur [13].
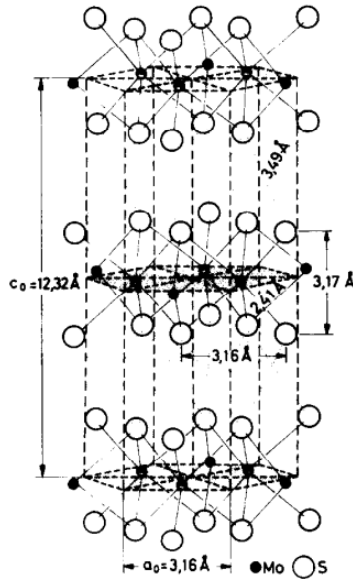
Figure 6: MoS_2 layered crystal structure reproduced from [13]

Due to the high polarity of the sulfur atoms, MoS_2 easily absorbs water molecules depending on the amount of moisture present from humidity. The water molecules will form hydrogen bonds and fit into the space between the layers of MoS_2 [12,13]. The wires are typically cleaned with acetone after the drawing process to remove contaminants, but there still may be traces of MoS_2 or other contaminants. If MoS_2 is still present on the wire after cleaning, it is possible that moisture is present on the wire as well. The presence of moisture on the surface of the wire is an obvious source of hydrogen entering the system.

Baseplate Contamination

From the previously mentioned porosity study conducted by Martukanitz et al., the base metal was found to have less of influence on porosity, but still had an effect of approximately 5-10% compared

to the 90% influence of the filler material [10]. Similar to the potential sources of hydrogen in the wire, sources in the base metal could be due to contaminants on the surface or in the bulk of the material.

A pre-deposit melting pass is common in the Sciaky EB-DED process. This pass de-focuses the beam and is intended to heat up and remove contaminants from the deposit surface of the base plate. By removing surface contaminants through the pre-deposit melting pass, it is expected that less porosity would be produced as compared to deposits on as-received base plates. The experiment conducted by the Applied Research Laboratory, evaluated a direct comparison between single pass deposits on as-received base plates to single pass deposits on pre-deposit melting pass base plates. Observations of this comparison showed that all four wires evaluated in this experiment produced less porosity in the single pass pre-deposit melt pass condition [11].

Atmospheric Contamination

The final potential physical source of hydrogen within the system is identified as the presence of hydrogen in the atmosphere. Martukanitz et al. evaluated gas metal arc welding, where hydrogen in the welding arc was identified as a potential source of hydrogen entering the system [10]. The results determined that hydrogen in the welding arc had the smallest influence on porosity, on the order of 0.01-0.015%. This effect is small relative to the approximately 90% influence from the wire and 5-10% influence from the base metal. As mentioned before, the EB-DED process is conducted under high vacuum to avoid electron scattering due to collisions with molecules in the air. Since the molecules in the air are at a minimum, this indicates a similar influence on porosity from atmospheric contamination as the gas metal arc welding experiment [14,15].

Back streaming contamination is a common problem among vacuum pumping systems and occurs when the diffusion oil travels in the opposite direction of the intended flow. This causes the pumping oil to enter the vacuum chamber, since the fluid in the pump has a higher potential of becoming entrapped and pulled into the chamber due to differences in pressure. The introduction of hydrocarbons from oil back streaming creates a potential source of contamination in the system. Back streaming is likely to occur in a system when the vacuum pump becomes too hot as a result of low or no coolant, high coolant temperatures, or leaks in the pump or system [16,17]. The best solution to negate back streaming is to incorporate a sub-refrigerated cold trap into the system between the diffusion pump and the vacuum chamber. The trap condenses the hydrocarbon vapor and collects it before it can reach the chamber, reducing but not eliminating back streaming contamination [17].

Aluminum Vaporization

In an experiment conducted by Chen et al., an unusual pore morphology was identified from electron beam-based DED processing of Ti-6Al-4V [18]. The new pore morphology has a near-spherical shape with a ripped inner surface and a similar size to the typical gas induced spherical porosity. This unique surface profile is argued to be formed from aluminum vapor becoming trapped in the melt during solidification. Due to the different inner pore surfaces, the formation mechanism for smooth surfaces and ripped surfaces must be different. However, since the gas induced pores and ripped inner surface pores have a similar size and shape, there may be a connection between the two types of pores [18].

a)   b)
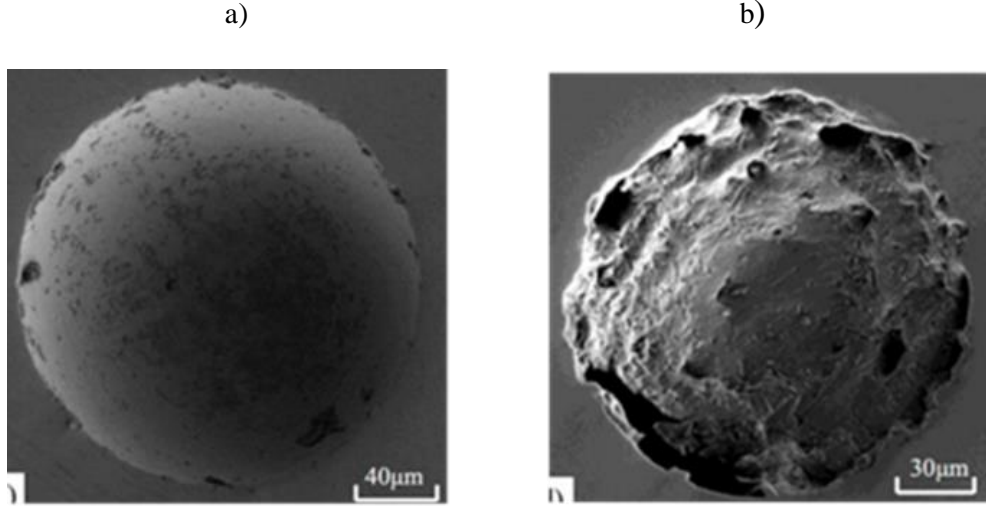
Figure 7: SEM images of a smooth spherical pore (a) and spherical pore with a ripped inner surface (b)

Energy dispersive spectroscopy (EDS) was used to characterize the composition of the pores at the inner surfaces and the deposition zone next to the pore. Using an average of multiple probes, it was found that the aluminum composition dropped from 5.92% in the base material near the pore to 3.8% on the inner surface of the pore. The decrease in aluminum content on the inner surface of the new pores suggests that the ripped surface could be the result of an evaporation process [18]. Using Equation 1, the vapor pressure of aluminum is calculated to be approximately three orders of magnitude higher than titanium and vanadium in the melt [19].

$$\log(P[atm]) = A + \frac{B}{T} + C * \log(T) \qquad (1)$$

where the material constants A, B, and C for aluminum, titanium and vanadium are listed in Table 1 and T is in Kelvin.

Table 2: Material constants for Al, Ti, and V [19]			
Element	A	B	C
Aluminum	5.911	-16211	-0.7927
Titanium	6.358	-22747	-1.3376
Vanadium	6.929	-25011	-0.5501

This suggests that the evaporation of aluminum could be the cause of the formation of the pores with a ripped inner surface. Figure 6 shows the vapor pressures for aluminum, titanium, and vanadium over the range of 1000 K to 2400 K [19].
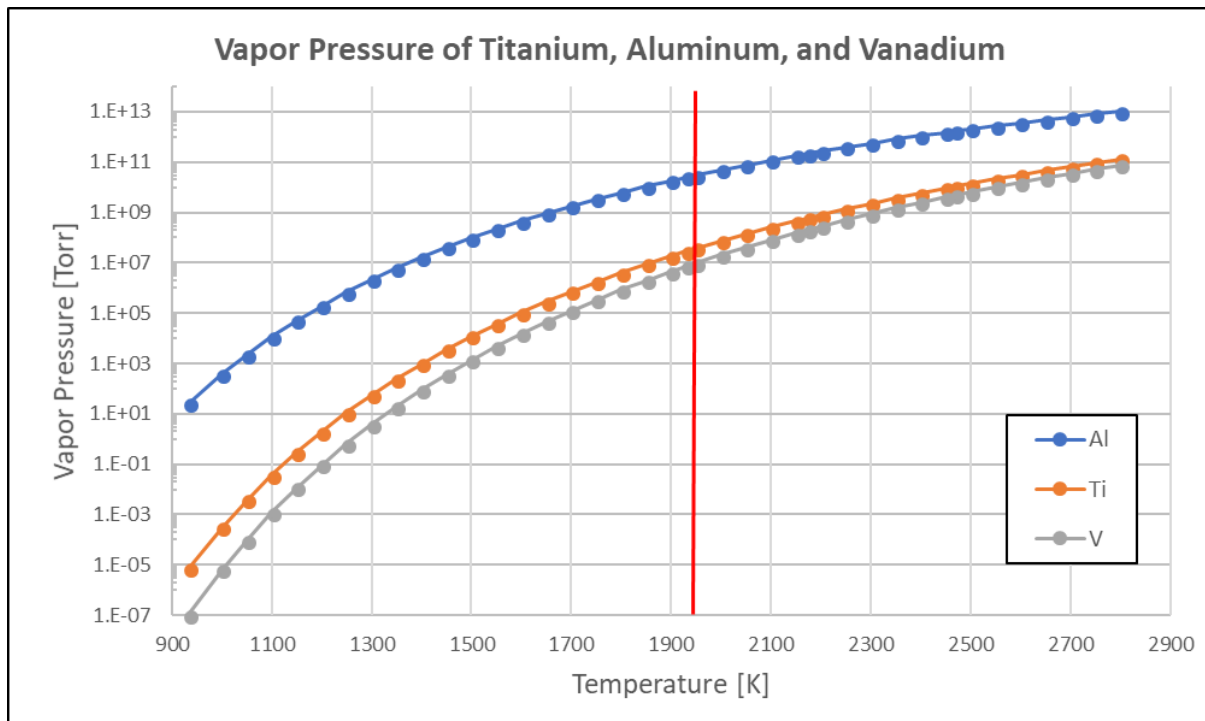
Figure 8: Vapor pressure of titanium, aluminum, and vanadium as a function of temperature

Line energy is defined as the energy input divided by the scan speed of the process. For EB-DED, the line energy can be calculated using Equation 2 [20].

$$\text{Line Energy} = \frac{(\text{Beam Current} \times \text{Voltage})}{\text{Scan Speed}} \qquad (2)$$

Line energy can be split into two main categories for evaluation, energy input and scan speed. Figure 9 represents two plots showing the effect of scan speed and beam current on final part density [20]. The line drawn across both plots signifies the theoretical density for Ti-6Al-4V. Slower scan speeds produce the highest densities, and the density decreases as the scan speed increases. Scan speeds lower than 5 m/s with a beam current of 15 mA yield densities greater than the theoretical density for Ti-6Al-4V, which is likely due to evaporation losses of aluminum. As the beam current increases the density increases, given a constant scan speed of 6 m/s. Beam currents greater than 25 mA produced part densities greater than the theoretical density, which is likely due to evaporation losses of aluminum. Based on Equation 1, high line energies can be created from either a low scan speed, high beam current, or both. In both cases, low scan speed and high beam currents, densities higher than the theoretical are produced due to evaporation losses of aluminum. This should not be confused with a higher density part due to lower amounts of porosity [20].
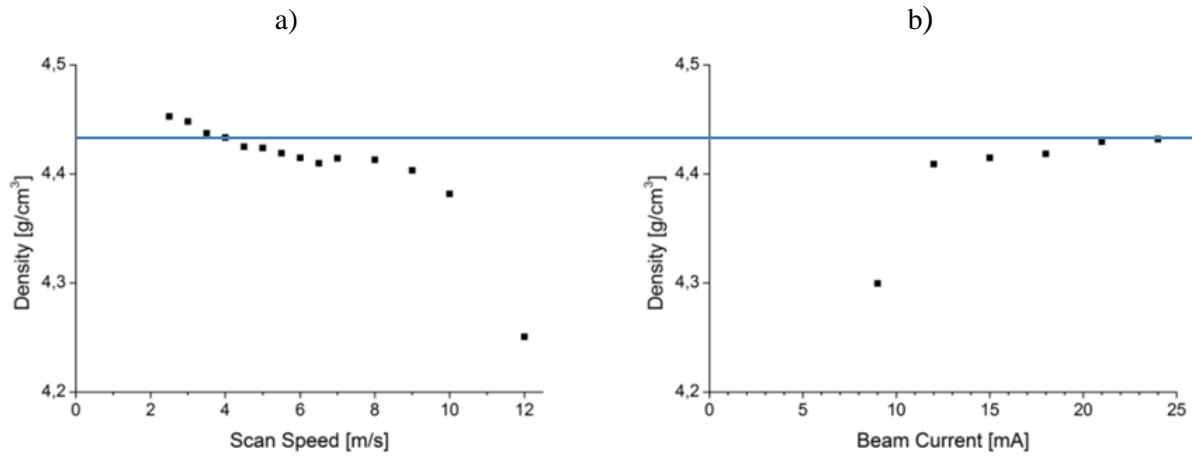
Figure 9: Effect of scan speed (a) and beam current (b) on part density reproduced from [15]

The energy input for an EB-DED process is determined by multiplying the current of the beam by the accelerating voltage applied to the freed electron [20]. In an electron beam AM process, typical values for the current and voltage are on the order of 235 mA and 40 kV, respectively. These values would generate an energy or power input of 9.4 kW. This energy input is very high compared to laser-based AM processes, which typically use energy inputs between 200 W and 2 kW. The high energy input of the electron beam process creates issues due to evaporation of low vapor pressure alloying elements. As the energy input increases, the evaporation losses increase at an exponential rate [15,20].

Process Parameters

Controlling the process parameters can influence the lifetime of the melt pool, which has an effect of the degree of porosity formed [21]. This can be explained by classical bubble nucleation theory, where occurrence of porosity can be broken down into three steps: bubble formation, growth, and escape.

Different beam scan speeds can alter the amount of porosity produced based on this three-step process. Bubble formation, or nucleation, requires the establishment of a liquid-gas interface, which leads to an increase in free energy within the system. Given a high concentration of hydrogen, homogenous nucleation is likely to occur at the center of the melt pool. Heterogeneous nucleation is likely to form at the liquid-solid interface, where the interface provides a surface for nucleation to occur. As the nucleation of hydrogen gas bubbles continues, the concentration of hydrogen in the liquid around the bubble decreases and creates a composition gradient. The generated gradient drives diffusion from hydrogen rich regions in the melt towards the bubble and promotes bubble growth. If the conditions allow, the bubble continues to grow as it floats in the melt pool and eventually escapes. In order for this to happen, the liquid metal must have high fluidity and low pressure for the bubble to float to the surface. Although, the bubble may still become trapped if the surface of the melt solidifies before the bubble has enough time to escape [22]. Mohandas et al. evaluated the effect of scan speed on the amount of porosity [20]. Porosity was observed to be at a minimum for high and low scan speeds, and at a maximum for intermediate scan speeds. At high scan speeds, the lifetime of the melt pool is short and the temperature of the melt is low compared to slow and intermediate scan speeds. These conditions are unfavorable for bubble nucleation and therefore porosity has a low tendency to form during high scan speeds. At low scan speeds, the melt pool will have a long lifetime and reach a high temperature relative to a high scan speed. This allows sufficient time and ideal melt pool conditions to allow bubble nucleation, growth, and escape, limiting porosity formation during low scan speeds. At intermediate scan speeds, the conditions

allow bubble nucleation and growth, but are not sufficient enough for the bubble to escape. Figure 10

shows the relationship between the beam scan speed and porosity formation in the deposit [20].
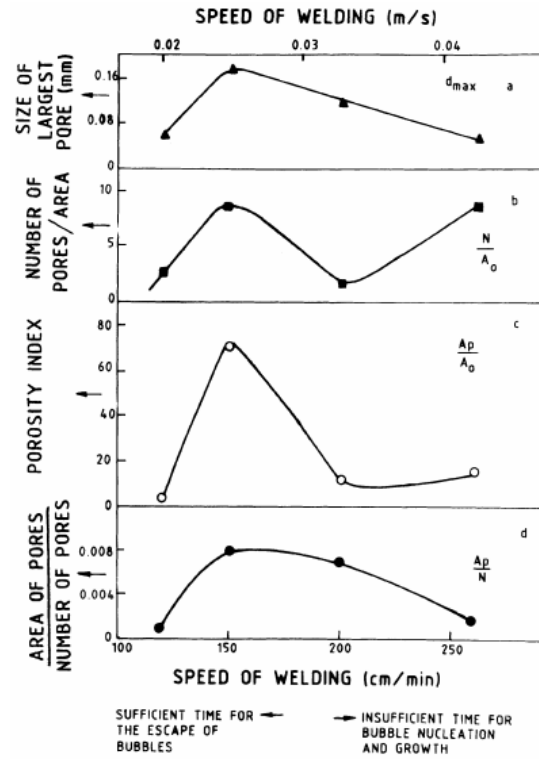
Figure 10: Effect of scan speed on porosity reproduced from [20]

Chapter 3: Experimental Procedure

The goal of this experiment was to evaluate the effect of potential sources of porosity on the degree of porosity. Potential sources of porosity were identified during the literature review and were then related to variables in the process. The first section of this chapter describes the experimental variables that were selected and their expected effect on porosity. Next, a full factorial design of experiment (DOE) was selected to include all of the run combinations, as well as additional replication runs. Each combination of variables was only run once (or twice for replication runs), so large samples were built so that multiple samples could be cut from each build to increase the amount of available data.

Experimental Variables

Wire Alloy – Aluminum Content

The first experimental variable of interest is the effect of aluminum content on the degree of porosity. The combination of high energy density from the electron beam and low vapor pressure of aluminum, suggests that aluminum is easily vaporized during this process. The vaporized aluminum bubbles in the liquid metal could become trapped during solidification resulting in porosity. These pores are expected to have a spherical morphology, typical of gas evolution, but may have a rough inner surface as suggested by Chen et al. [18]. To determine the potential effect of aluminum content on the degree of porosity, filler wires with different aluminum contents were selected. Ti-6Al-4V was the initial material of interest for this study, and the 6% aluminum content in this alloy was compared to no aluminum

content in CP-Ti. Given this information, it is expected that Ti-6Al-4V will produce higher levels of porosity due to the vaporization of aluminum.

Wire Quality – Hydrogen in the System

The next experimental variable of interest is the wire quality, specifically the level of contamination from H, S, F, and N. When considering an AM system, there are three main components to consider as potential sources of contamination; the deposit material, baseplate, and atmosphere. Results from Martukanitz et al. indicate that a majority of the porosity formed during welding aluminum resulted from contamination associated with the filler wire. In addition to this, the wire drawing lubricant, MoS_2, has a high polarity and easily absorbs moisture which may be a source of contamination into the system. Observing Mo or S on the surface of the wire may indicate residual drawing lubricant which could be acting as a source of hydrogen into the system. Furthermore, the solubility of hydrogen in titanium indicates that hydrogen may be rejected upon solidification, resulting in pores. Using the Inert Gas Fusion vacuum hot extraction (VHE) technique, hydrogen can be detected in the bulk of the sample down to 1 ppb H.

In order to test the effect of wire quality on the degree of porosity, at least two different wire qualities must be evaluated for each alloy. For this experiment, the relative qualities of the wire were of interest, not just the level of sulfur or hydrogen contamination, so surface and bulk chemical analyses were conducted. The XPS, SEM and EDS techniques were used to evaluated S, F, and N on the surface of the wire, and VHE methods were used to evaluate H, N, and S within the bulk of the wire. The results of the characterization techniques on all four wires used are reported in Table 3. For the CP-Ti wires, it is

clear from the surface and bulk results that Wire D has lower levels of overall contamination compared to CP-titanium Wire E. When comparing the Ti-6Al-4V wires, there is no obvious wire with higher levels of contamination, even when just looking at the surface or bulk results. Since the quality of Wire B and C was difficult to rank, the level of hydrogen contamination was chosen to represent the wire qualities due to its possible influence on pore formation.

Table 3: Wire surface and bulk chemical analysis

Filler Material		XPS: Surface			VHE: Bulk		
Alloy	Wire ID	S	F	N	H	N	S
Ti-6Al-4V	Wire B	1 ± 0.1 at %	1 ± 0.4 at %	2 ± 0.5 at %	15.6 ppm	70 ppm	< 5 ppm
Ti-6Al-4V	Wire C	0	0	3 ± 0.7 at %	19.6 ppm	54 ppm	< 5 ppm
CP-Ti	Wire D	0.3 ± 0.2 at %	0	2.9 ± 1.9 at %	14.4 ppm	50 ppm	< 5 ppm
CP-Ti	Wire E	0.7 ± 0.1 at %	0	6.7 ± 0.3 at %	32.4 ppm	50 ppm	< 5 ppm

In addition to the quantitative results from the XPS and VHE methods, qualitative results on the surface topography and chemical composition maps were obtained from SEM and EDS. Since wires with a greater surface roughness may be more difficult to clean, surface roughness may impact the level of residual contaminants. The SEM and EDS techniques were used to determine surface roughness of the wire and identify possible contaminates present on the wire surface. Figure 11a shows an SEM micrograph with 3 corresponding EDS composition maps at increasing magnification (Figure 11b-d). The SEM results show that the wire surface appears smooth, with no cracks, voids, or other rough features. The EDS composition map results shows a near uniform distribution of sulfur in Figure 11b,

but it is clear in Figure 11c and 11d that sulfur is present on the wire surface in clusters. Alone these

sulfur clusters are of interest, but they could also suggest residual MoS_2 on the wire surface resulting in

possible moisture or other contaminants entering the system.
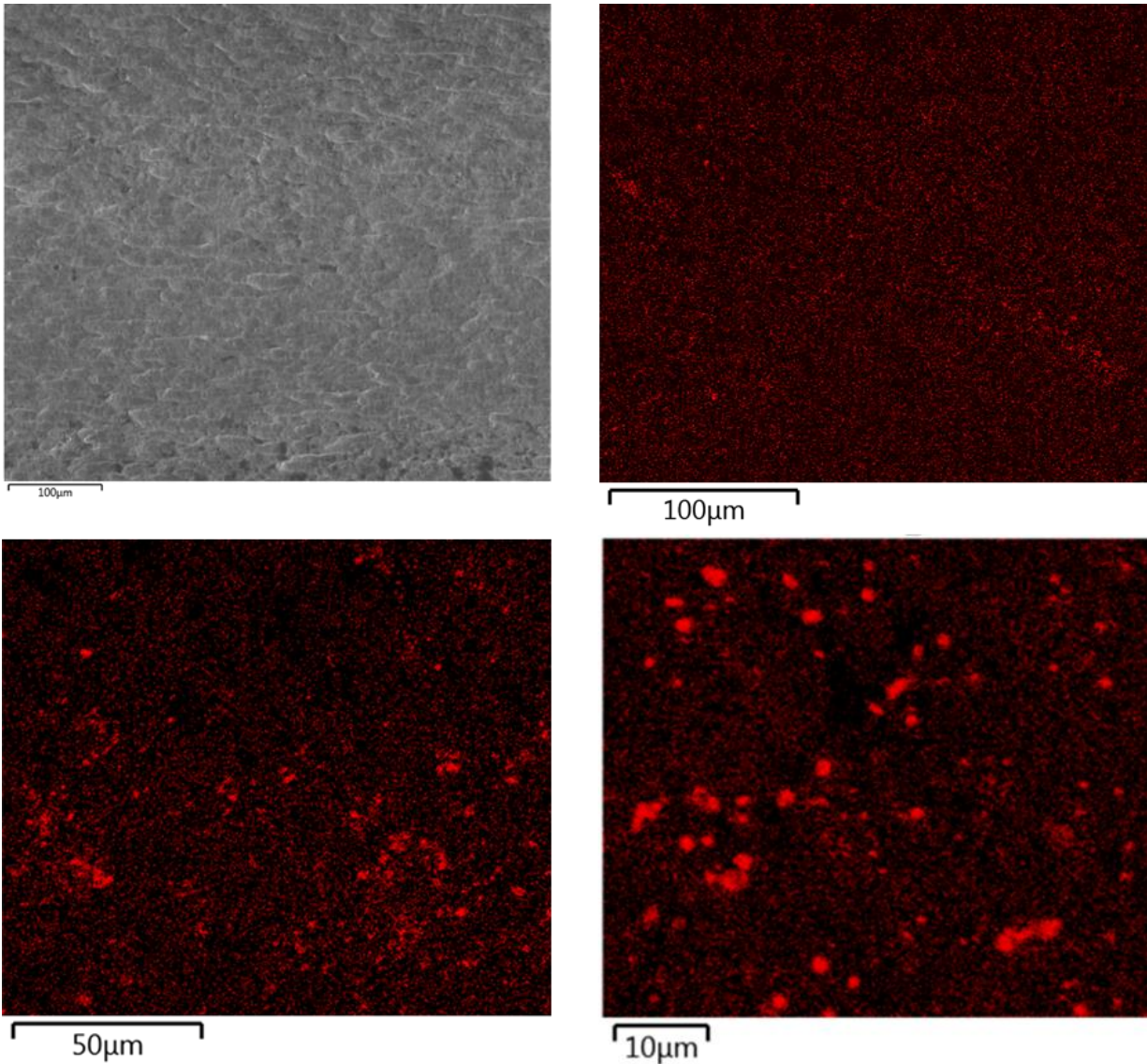
Figure 11: SEM micrograph (a) and EDS images of sulfur clusters on the surface of wire (b-d)

Process Parameter – CLC vs Fixed

The melt pool lifetime affects the extent of porosity formation, which in turn determines the degree of porosity. Intermediate melt pool lifetimes favor a higher degree of porosity compared to shorter or longer melt pool lifetimes. An easy way to manipulate the melt pool characteristics (e.g. size, lifetime, T, etc.) is by altering the process parameters that influence the energy density of the beam. This can be done effectively by applying a CLC feature that can alter process parameters based on a response during the process. The CLC feature used in this experiment incorporates a dynamic raster to control the energy density of the beam to maintain a consistent melt pool size. This parameter setting was tested against a fixed parameter setting, where the initial process parameters in Table 4 were used throughout the entire deposition process. The CLC feature is expected to produce lower levels of porosity compared to the fixed parameter settings.

Table 4: Initial Process Parameters	
Vacuum Level	20-50 µTorr
Accelerating Voltage	40 kV
Beam Current	235 mA
Scan Speed	30 in/min
Wire Feed Rate	127.3 in/min (1/8" dia.)
Raster	9 ring pattern at 600 Hz

Design of Experiment

2-level Full Factorial with Replications

There were several potential variables to select from the literature review, so three variables were selected to be evaluated using a 2-level full factorial experiment. The variables were selected based on their expected impact on porosity, where the two levels of the variable would have the greatest difference in porosity. The experimental design of a two-level factorial experiment with three variables would have 8 runs, but 4 replication runs were added for repeatability. Table 5 shows the run numbers for a given combination of wire alloy, wire quality, and process parameter settings used. The samples are split into groups of three with the same wire alloy and wire quality, but with different processing parameters. Each set of three has one run with fixed parameters and two runs with a closed loop control function. The experiment was not completely random due to the long pump-down time. As a result, all three builds for each wire were run consecutively and then the wire was swapped for the next three runs.

Table 5: Experiment Run Matrix

Run	Filler Wire Alloy	Alloy Quality	Process
Number	Ti-6Al-4V or CP-Ti	Hydrogen Contamination	CLC with Dynamic Raster vs. Fixed Parameters
1	Ti-6Al-4V	15.6 ppm (low)	Fixed
2	Ti-6Al-4V	15.6 ppm (low)	CLC
3	Ti-6Al-4V	15.6 ppm (low)	CLC
4	Ti-6Al-4V	19.6 ppm (high)	CLC
5	Ti-6Al-4V	19.6 ppm (high)	Fixed
6	Ti-6Al-4V	19.6 ppm (high)	CLC
7	CP-Ti	32.4 ppm (high)	CLC
8	CP-Ti	32.4 ppm (high)	CLC
9	CP-Ti	32.4 ppm (high)	Fixed
10	CP-Ti	14.4 ppm (low)	CLC
11	CP-Ti	14.4 ppm (low)	Fixed
12	CP-Ti	14.4 ppm (low)	CLC

Build Geometry

      To maintain simplicity within this experiment, a simple build geometry was designed and is represented in Figure 12. The initial build dimensions were designed to be 4 inches long by 1 inch wide by 2 inches in height. During deposition, the geometry was slightly altered to accommodate the selected build plan of 17 layers with 3 passes per layer and each pass was 5 inches in length. The new dimensions became approximately 5 inches long by 1.5 inches wide by 2.5 inches in height.
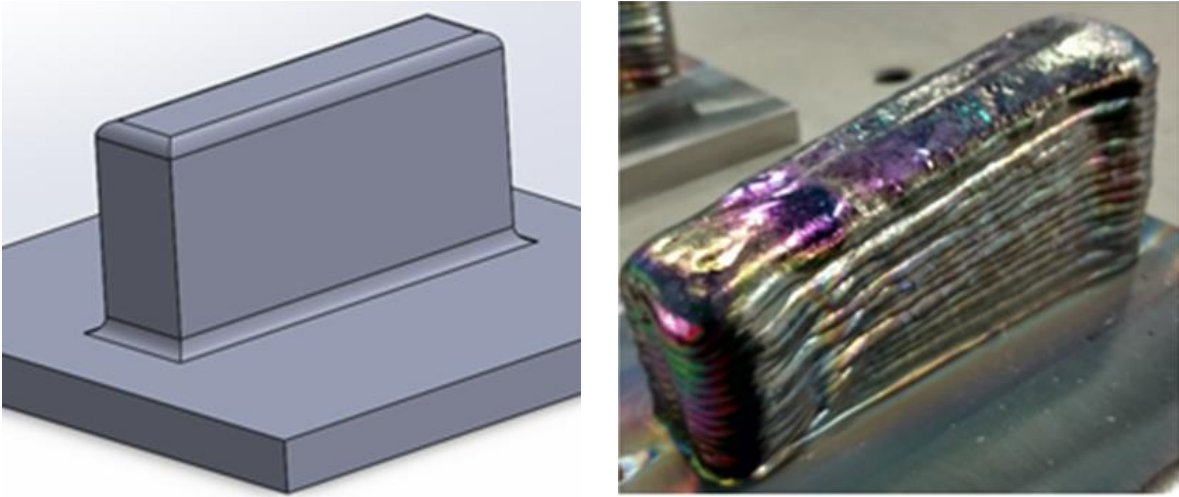
Figure 12: Initial build design (a) and final part geometry (b)

Chapter 4: Pore Characterization

Metallography

Optical Microscopy (OM) of cross sections is a useful technique for evaluating porosity, providing information on pore size and location in the sample, but it is limited to 2D. The deposits were prepared for OM by first cutting cross sections from the deposits along the scan direction to produce five sections from each sample. Figure 13a represents the full build before the sample was sectioned and Figure 13b represents the full build after it was sectioned. 0.5 inches were removed from the end of each build to eliminate unwanted end effects due to differences in initial and final scan speeds and energy input.

Since the samples were only cut into five sections to represent the entire part, there is statistical error involved with the microscopy analysis. To minimize the error, each sample was sectioned at a random distance along the build direction. The random distances were generated with MATLAB and are listed next to each sample and its corresponding surface in the Appendix. In Figure 13, the build direction moves from right to left on the sample. After discarding the ends of the sample, the first section on the right side was identified as Sample A. The next four samples were labeled as Sample B, C, D and E, respectively, moving from right to left. With respect to Figure 13, the right surface of each sectioned sample was chosen to be evaluated.

Once all of the samples were sectioned, the faces of interest were identified and then the samples were mounted in an epoxy cold mount. The samples were ground and polished by hand to prepare them for optical microscopy. The grinding process started with 60 grit sand paper and progressed

through 120, 240, 320, 400, 500, 800, 1000, 1200, and 2400 grit. The protocol for grinding started

with the sample in an initial orientation, then after 100 oscillations the sample was rotated 90°. This

process was repeated until the sample was ground for 100 oscillations in four different orientations.

After the grinding process was complete, the samples were polished using a 1 µm diamond suspension

polishing solution until the scratches were removed for optical microscopy.
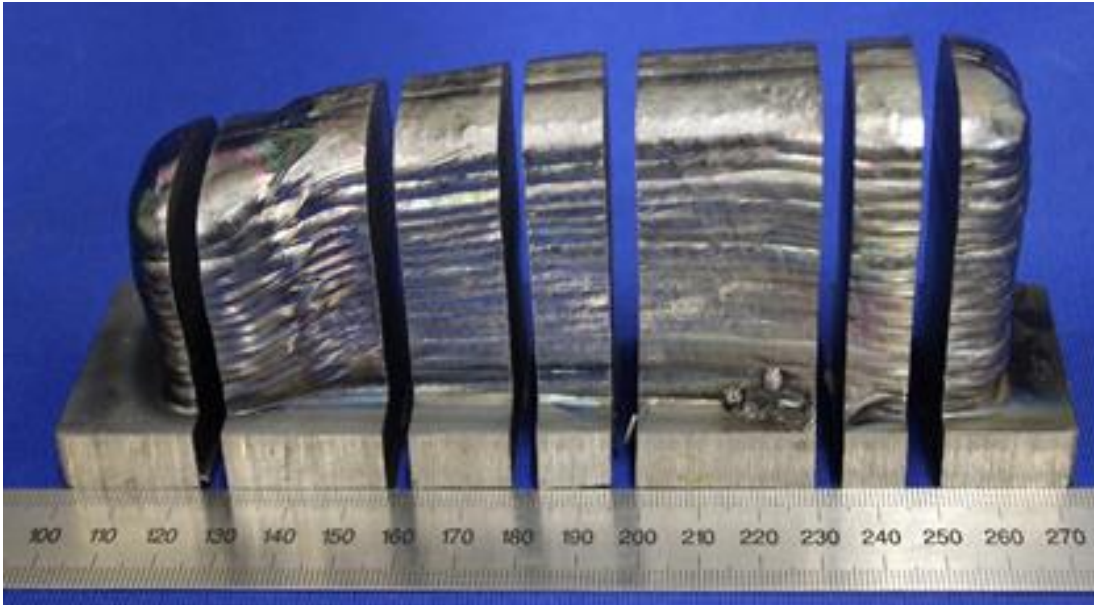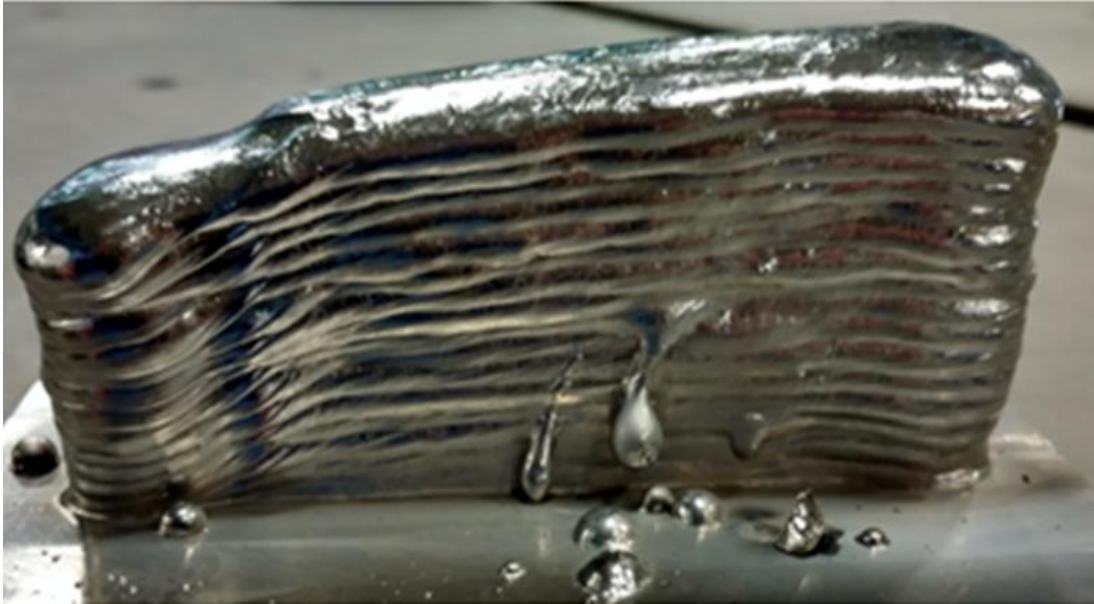
Figure 13: Final build before (a) and after (b) sectioning

Optical Microscopy

OM Scanning Procedure

The samples were viewed at 50x magnification and scanned for porosity following the process shown in Figure 14. As a pore was encountered, its diameter was measured and tabulated into defined size class ranges shown in Table 6. Figure 14b and 14c show where the interface region and deposit of the samples were separated.
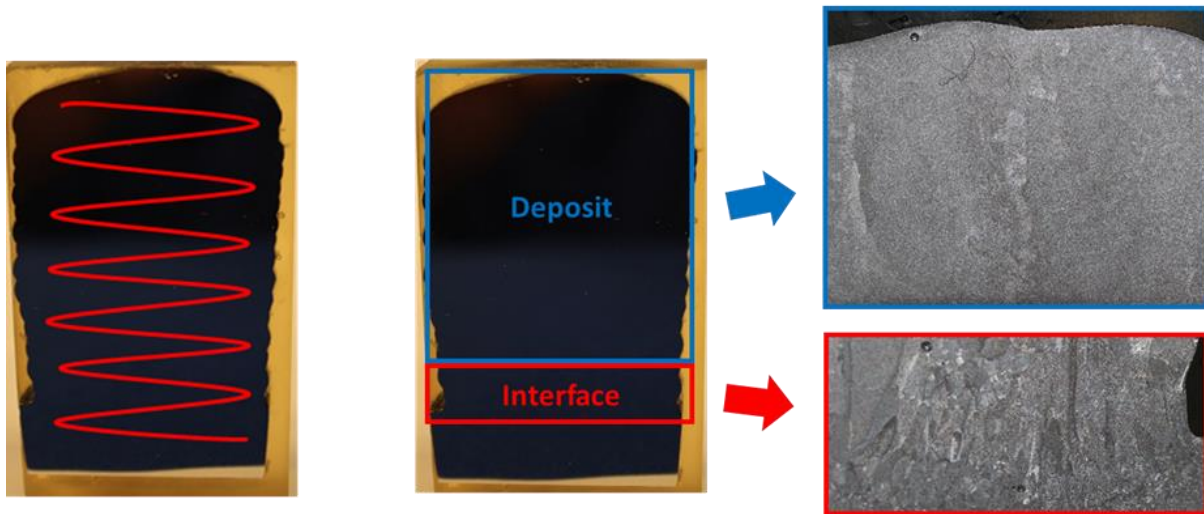
Figure 14: OM scanning procedure (a) and separation of the deposit and interface regions (b and c)

Table 6: OM pore characterization table						
	Interface			**Deposit**		
Size Class (μm)	**Round**	**Faceted**	**Elongated**	**Round**	**Faceted**	**Elongated**
0-49						
50-99						
100-149						
150-199						
200-249						
250-299						
300-349						
350-400						
>400						

In addition to size and location, different pore morphologies were observed. Three different pore morphologies were observed and each are represented by the micrographs in Figure 15. Figure 15a and 16b shows typical spherical pores observed in Ti-6Al-4V. Only 6 total counts of observed porosity in CP-Ti; all were less than 150 μm and located at the interface. Figure 15c and 15d are of elongated or lack of fusion pores observed in CP-Ti and Ti-6Al-4V samples. Elongated pores have large length to width ratio in the observed two dimensions and likely elongates in the third dimension as well (into the page). These are all likely to be lack of fusion pores (LOF), since they are located between the 3 passes in the layers. A final pore type, shown in Figure 15e and 15f, was identified and referred to as faceted pores. These pores do not have a smooth spherical or elongated LOF shape but are equiaxed with rough edges. It is important to note the uncertainty of the depth of all observed pores, since OM is limited to 2D. In addition to this, LOF porosity was not of interest for this study, so it was tabulated but not included any further in this report.
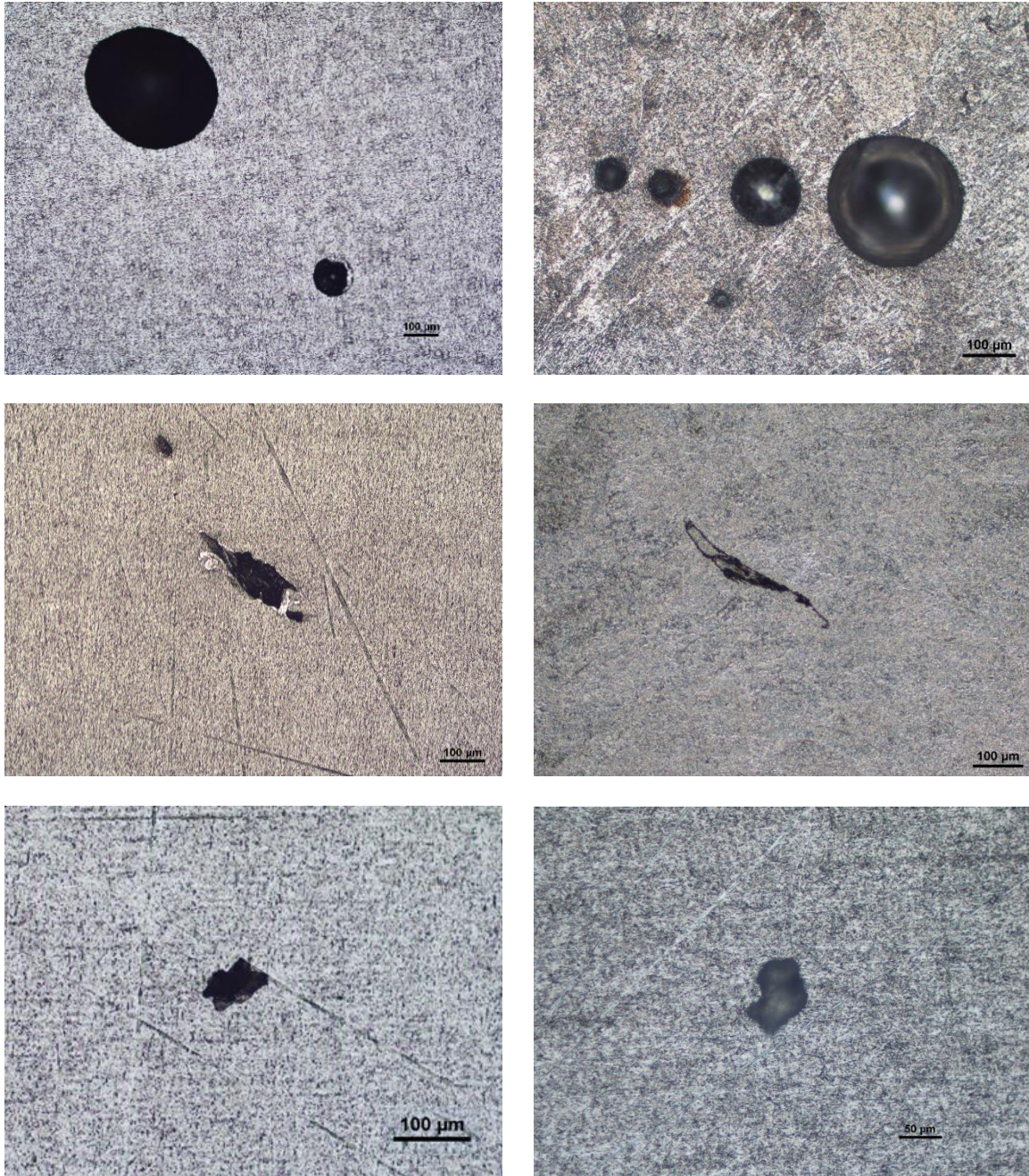
Figure 15: Micrographs showing typical spherical (a and b), elongated or LOF (c and d), and faceted (e and f)

OM Results

One of the samples evaluated was Sample 1C, deposited with the relatively lower hydrogen content

(15.6 ppm H) Ti-6Al-4V alloy filler wire. Table 7 lists the results for the size, location, and

morphology of the pores observed in Sample 1C. The scanned surface of the sample contained 15

spherical pores, 16 faceted pores, and 1 elongated pore all of varying sizes between 20 and >400 µm.

Figure 16a is a macrograph of the scanned surface, where large pores were identified in the interface

region and the first few layers of the deposit. Figures 16b-d are micrographs including spherical

pores and lack of fusion pores located in and near the interface region.

Table 7: Sample 1C Raw OM data						
	Interface			**Deposit**		
Size Class (µm)	**Round**	**Faceted**	**Elongated**	**Round**	**Faceted**	**Elongated**
20-49	2	0	0	0	12	0
50-99	3	0	0	2	2	0
100-149	2	0	0	1	2	0
150-199	2	0	0	0	0	1
200-249	0	0	0	1	0	0
250-299	1	0	0	0	0	0
300-349	0	0	0	0	0	0
350-400	0	0	0	0	0	0
>400	1	0	0	0	0	0
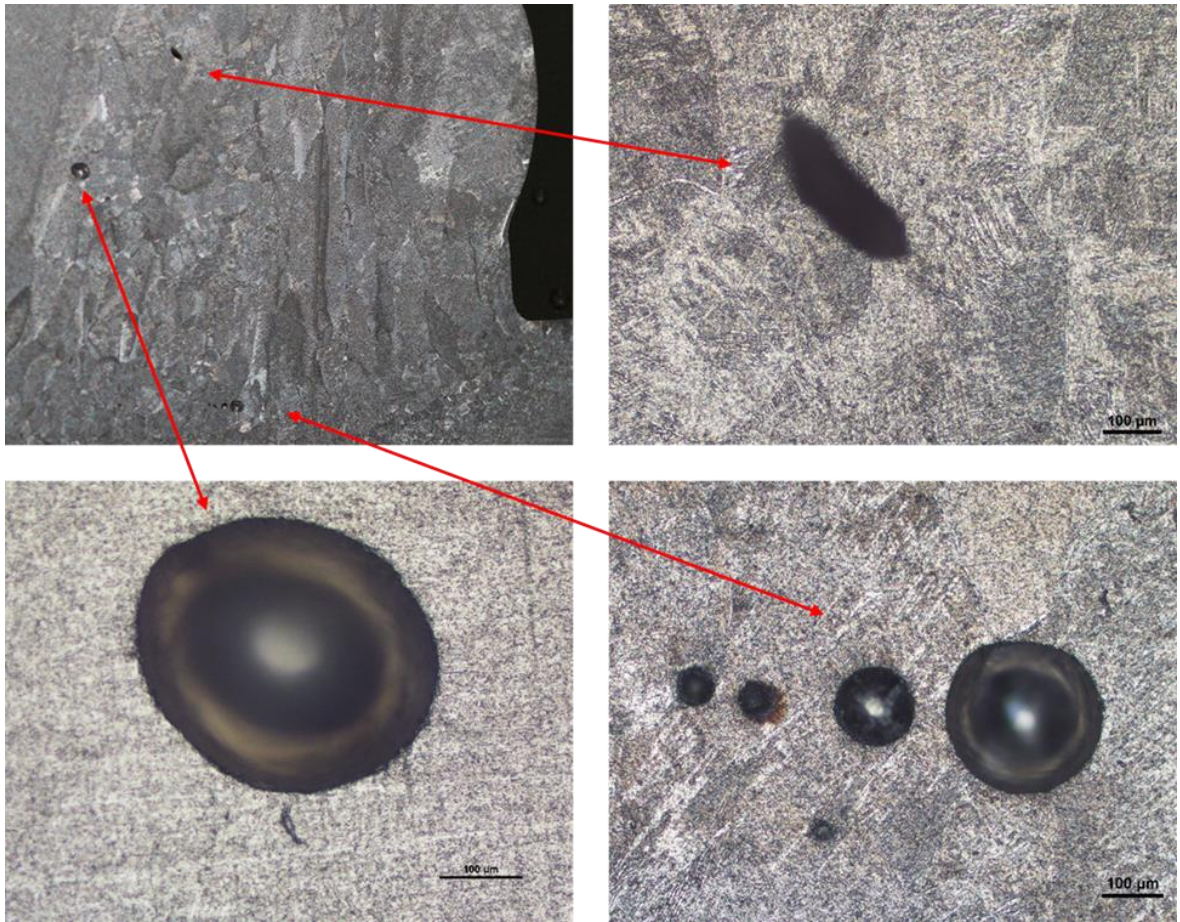
Figure 16: Macrograph of Sample 1C interface (a) with micrographs of observed pores (b – d)
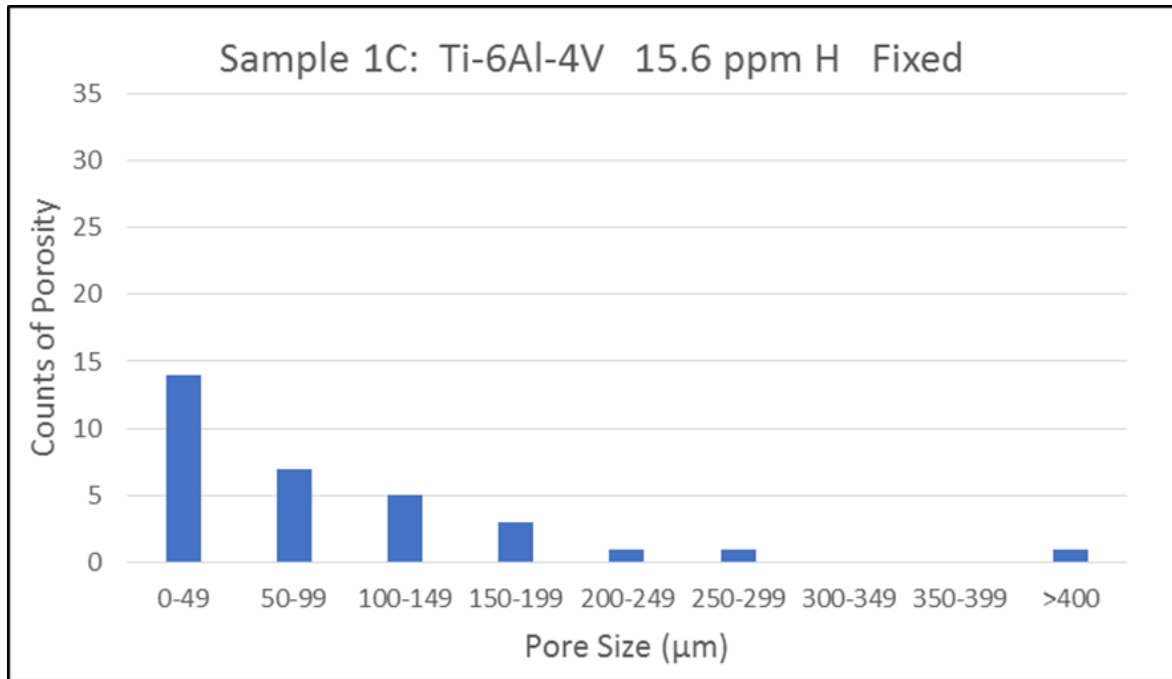
Figure 17: Total counts of spherical and faceted porosity in Sample 1C

Another sample evaluated was Sample 11B, deposited with the relatively higher hydrogen content (19.6 ppm H) CP-Ti filler wire. Table 8 includes the results for the size, location, and morphology of the pores observed in Sample 11B. The scanned surface of the sample contained 2 spherical pores, 55 faceted pores, and 8 elongated pores all of varying sizes between 20 and >400 µm. This is significantly less spherical porosity and more faceted and elongated than Sample 11B. Figure 17a is a macrograph of the scanned surface, with all three pore types observed in the interface region. Figures 17b-d are micrographs of the observed pores near the interface.

Table 8: Sample 11B Raw OM data						
	Interface			Deposit		
Size Class (μm)	Round	Faceted	Elongated	Round	Faceted	Elongated
0-49	1	7	0	0	12	0
50-99	1	5	0	0	7	1
100-149	0	2	0	0	5	3
150-199	0	1	0	0	4	2
200-249	0	0	0	0	4	0
250-299	0	0	0	0	0	0
300-349	0	0	0	0	4	0
350-400	0	0	0	0	2	0
>400	0	0	1	0	2	1

Figure 18: Macrograph of Sample 11B interface (a) with micrographs of observed pores (b – d)
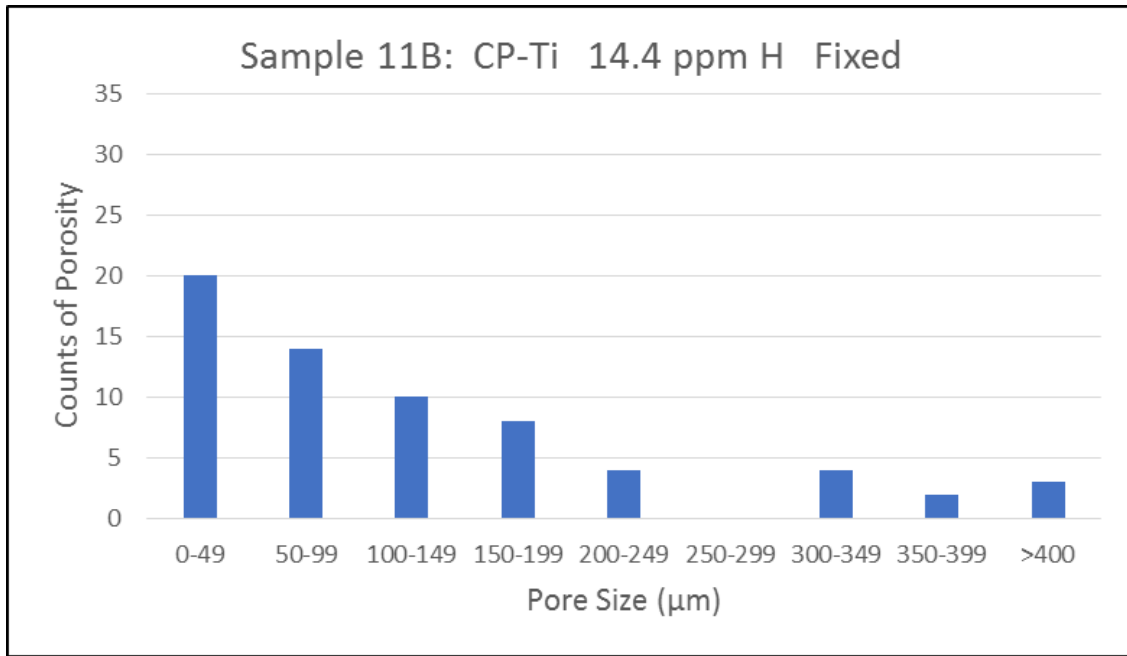
Figure 19: Total counts of spherical and faceted porosity in Sample 11B

Summary of OM Results

This pore characterization process was carried out for all samples and the results are reported in the Appendix. A few observations could be made from comparing the porosity data. To start, both Ti-6Al-4V and CP-Ti data sets all have a skewed distribution which can be observed in Figure 17 and 19. In addition, Ti-6Al-4V samples have less total counts of porosity (spherical and faceted) compared to CP-Ti. A majority of CP-Ti's porosity is associated with faceted pores, where only 6 total counts of spherical pores were observed in all 30 of the CP-Ti samples. In addition to this, it is important to point out that all spherical pores identified in CP-Ti were observed at the interface. This is important since all samples were deposited on Ti-6Al-4V baseplates, so the interface region of the CP-Ti samples are expected to contain small amounts of aluminum ($< 6\%$) and vanadium ($< 4\%$). A majority of the porosity

observed in Ti-6Al-4V was faceted, but there is significantly more spherical porosity compared to the CP-titanium samples.

Another notable observation is the relationship between filler wire hydrogen content and the degree of porosity. The level of porosity was expected to increase as the hydrogen content of the filler wire increases. The results show the opposite effect, where samples deposited using higher hydrogen content wire produced higher levels of porosity. This can possibly be explained since the hydrogen content listed for each sample only accounts for the hydrogen contribution from the wire and no other potential sources such as the baseplate or the atmosphere. As mentioned in the literature review, back streaming contamination is a common issue when continuously running oil diffusion vacuum pumps. Since the pumps were left running longer than usual at a lower efficiency, back streaming contamination is expected to increase the hydrogen contamination in the system. This source of hydrogen was un-accounted for and may affect the level of porosity.

Stereology Correction Method

General 2D to 3D Statistical Normalization

Optical microscopy is commonly used to characterize porosity since size, shape, and location of the pores can be obtained. Similar to the process described above, polished sections of the material are scanned for pores which are classified based on their size, morphology, and location in the build. This technique is attractive due to its simplicity, but the data acquired from this method is limited to two dimensions. A simple way to generate three dimensional values from the OM data would be to convert

the observed circle radius directly to the pore radius to calculate the volume. These calculated volumes

are not accurate since this assumes that each observable pore was cut through the center, or maximum

radius. Typically, the diameter of the observed circles is not equal to the actual diameter of the pore, as

seen in Figure 20. The accuracy of the calculation can be improved by accounting for the location of the

cut through the pore. This is done using a stereology correction method, which considers the location of

the cut within the pore and statistically normalizes the observed circle diameters to calculate a 3D size

distribution [23-25].
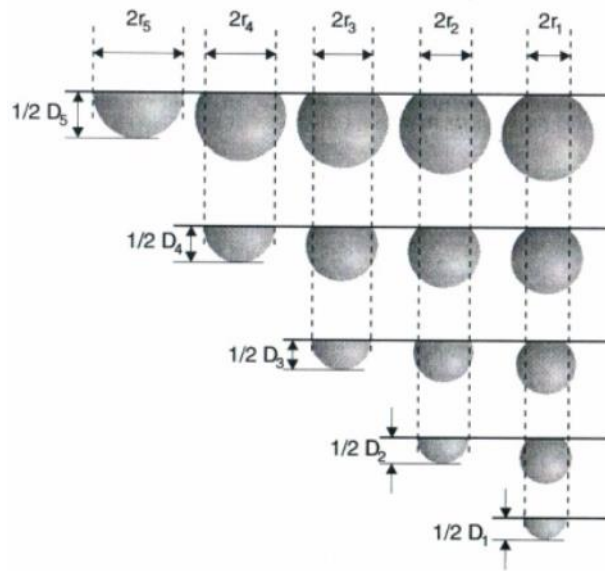
Figure 20: Pore class sizes (Di) and observed radius (ri) [25]

Scheil-Saltykov Correction Method

The Scheil-Saltykov correction method is commonly used since it is a simplified stereology

correction technique [23]. This method is applied to the experimental data since it allows the calculation

of a real size distribution of pores from metallographic micro-sections. In order to apply this stereology

method, a few assumptions are made; the material of interest consists of spherical pores with various

diameters in a statistical arrangement in the volume. Next, the maximum observed diameter ($n_A max$) is

set to be equal to the theoretical maximum pore size ($n_V max$). The observed circles are then separated

into N_s size classes, starting with 0 and going to ($N_s - 1$). The size classes will range from 0 to ($n_A max$)

with a constant class interval width (Δ). A pore with class size i, can be observed as a circle in the

categories between 1 and i, since the circle radius cannot exceed the actual pore radius, but may be

smaller.
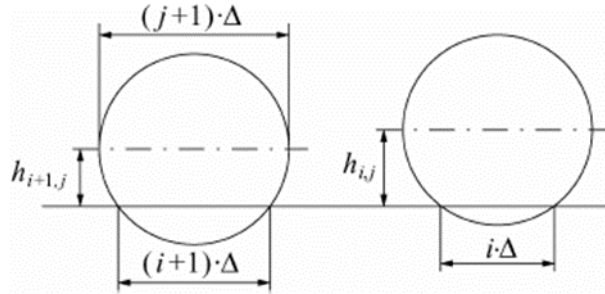
Figure 21: Planar cross sections of pores of pores in size group j with observed 2D pore size i.

The first step in this correction method is to determine the number of circles of size class i per

area:

$$(n_A{}^{s_i}) = \Sigma_{j=i}^{N_s-1} n_A{}^{s_{i,j}} \qquad (3)$$

This can be done by summing the number of circles of size class i which result from pores of j size class

($n_A{}^{s_{i,j}}$). From Figure 21, circles of size class i have diameters between i*Δ and (i+1)*Δ when a pore of

size class j is sectioned at a distance between $h_{i,j}$ and $h_{i+1,j}$ from the center of the pore. The length from

the center of the pore to the cut surface can occur on both sides of the pore, so ($n_A max$) can be represented

by the following equation:

$$(n_{A}{}^{s_{i,j}}) = 2\, n_{V}{}^{s_{i,j}}\,(h_{i,j} - h_{i+1,j}) \qquad (4)$$

where $h_{i,j}$ and $h_{i+1,j}$ are geometrically calculated based on Figure 21, as follows:

$$h_{i,j} = \frac{\Delta}{2}\sqrt{(j+1)^2 - i^2} \qquad (5)$$

$$h_{i+1,j} = \frac{\Delta}{2}\sqrt{(j+1)^2 - (i+1)^2} \qquad (6)$$

To simplify the expression for $(n_{A}{}^{s_{i,j}})$, a dimensionless value for the distance is defined as:

$$A_{ij} = \frac{2}{\Delta}\,(h_{i,j} - h_{i+1,j}) \qquad (7)$$

Substituting Equations 4-7 into Equation 3 and re-arranging yields:

$$(n_{A}{}^{s_i}) = \Delta * \Sigma_{j=i}^{N_s-1}\, n_{V}{}^{s_j} A_{ij} \qquad (8)$$

The resulting set of equations is in the upper triangular matrix form, and therefore they can be solved

recursively starting with the largest class size i:

$$(n_{A}{}^{s_i}) = \Delta * \left(n_{V}{}^{s_i} A_{ii} + \Sigma_{\substack{j=i \\ =1}}^{N_s-1} n_{V}{}^{s_j} A_{ij}\right) \qquad (9)$$

and the volumetric size distribution of the pores in the volume can be written as:

$$(n_{V}{}^{s_i}) = \frac{1}{A_{ii}}\left(\frac{n_{A}{}^{s_i}}{\Delta} - \Sigma_{j=i+1}^{N_s-1} n_{V}{}^{s_j}\right) \qquad (10)$$

The calculated size distribution is then converted to determine the number and total volume of

pores for each size class within the volume of material. Typically, porosity measurements are recorded in

units of volume of pores per mass of material, and in this experiment the level of porosity is recorded as

milliliters of pores per 100 grams of Ti-6Al-4V or CP-Ti. All equations in this section were reproduced from [23].

Sample Calculation

The following is a sample stereology calculation from the data showing the steps for calculating the 3D size distribution of pores organized into a table. First, the dimensions of the sample must be initially input, since the area of the micro-section and total volume of the sample are required for the calculation. Next, the number of pores per area of the sample is calculated by dividing the number of pores corresponding to each class size by the area of interest for that sample. Then, this value is statistically normalized by multiplying by the dimensionless quantity, $A_{i,j}$, to produce the total number of pores per volume. With this, the total number of pores, total volume of pores, and ultimately the volume of porosity per mass of metal can then be determined. Table 9 summarizes the stereology calculations described in this section.

Table 9. Sample calculation for the Scheil-Saltykov stereology correction method						
Class Size [μm]	#Pores	#Pores/Area [cm^{-2}]	#Pores/Volume [cm^{-3}]	#Pores	Volume of Pores [cm^3]	Porosity [mL/100 g]
0-49	10	0.539	34.085	1606.8	1.315E-05	1.011E-06
50-99	13	0.700	62.669	2954.3	6.526E-04	9.232E-05
100-149	6	0.323	17.762	837.4	8.563E-04	3.433E-05
150-199	4	0.216	10.532	496.5	1.393E-03	3.313E-05
200-249	2	0.108	2.302	108.5	6.471E-04	3.362E-06
250-299	3	0.162	6.915	326.0	3.550E-03	5.541E-05
300-349	2	0.108	5.678	267.7	4.811E-03	6.167E-05
350-399	0	0.000	0.000	0.0	0.000E+00	0.000E+00
>400	1	0.054	2.523	118.9	3.985E-03	2.269E-05

Stereology Results

The Scheil-Saltykov stereology conversion method was applied to all of the samples, and the results are summarized in Figure 22. Note that the values reported for the CLC runs are an average since each had a replication run. From the stereology conversion results, it is difficult to relate the experimental variables to the volume of porosity. There is an expected effect on the degree of porosity based on aluminum content, hydrogen contamination, and pore location based on the OM results so, the individual effects from the experimental variables were evaluated to further understand the data.
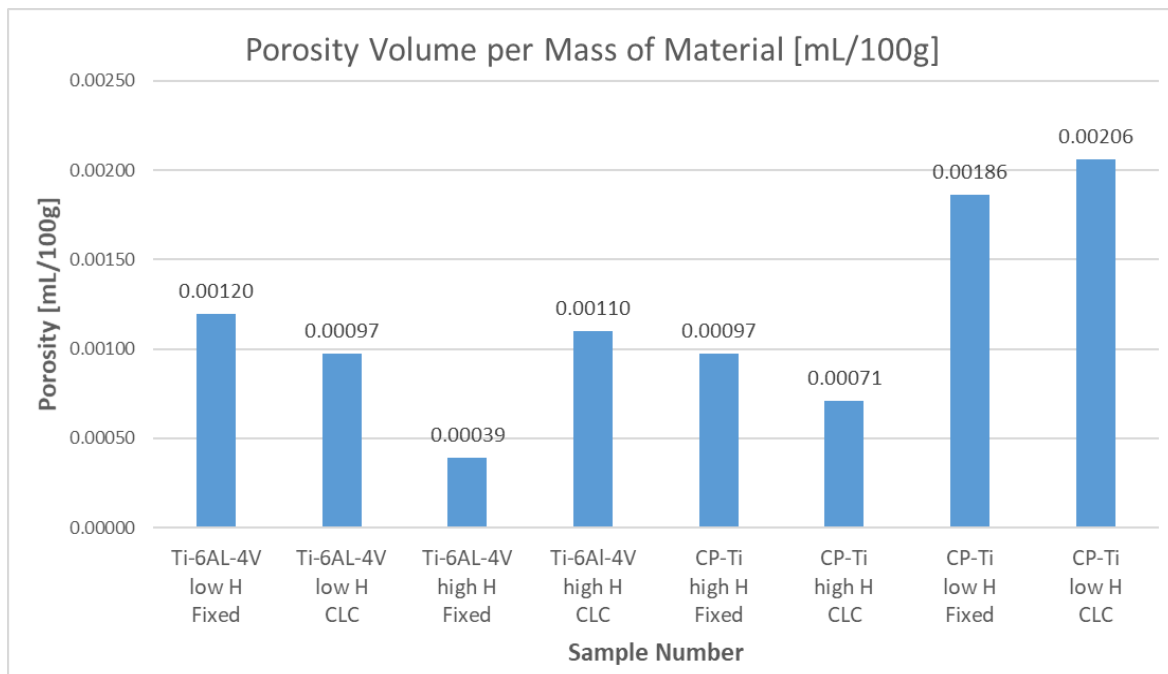
Figure 22: Stereology calculation results of total porosity levels (spherical and faceted) for each run combination

Stereology: Aluminum Content and Pore Morphology

Figures 23 and 24 report the stereology results which are separated by alloy into Ti-6Al-4V and

CP-Ti. Comparing these two plots shows a greater amount of total porosity in CP-Ti samples compared

to Ti-6Al-4V, which agrees with the OM results. Furthermore, when this data is separated by pore

morphology into spherical and faceted porosity, there is a greater amount of faceted porosity observed in

the CP-Ti samples and greater amounts of spherical porosity observed in the Ti-6Al-4V samples. This

can be seen by comparing Figures 25 and 26 for spherical pores and Figures 27 and 28 for faceted pores,

and also agrees with the results from OM. This further supports that an alloying element, likely

aluminum, plays a role in spherical pore formation. This could be due directly to aluminum vaporization

or the elements effect on the properties of titanium. In addition, the stereology results also showed a

decrease in porosity for samples deposited with higher hydrogen content wire.
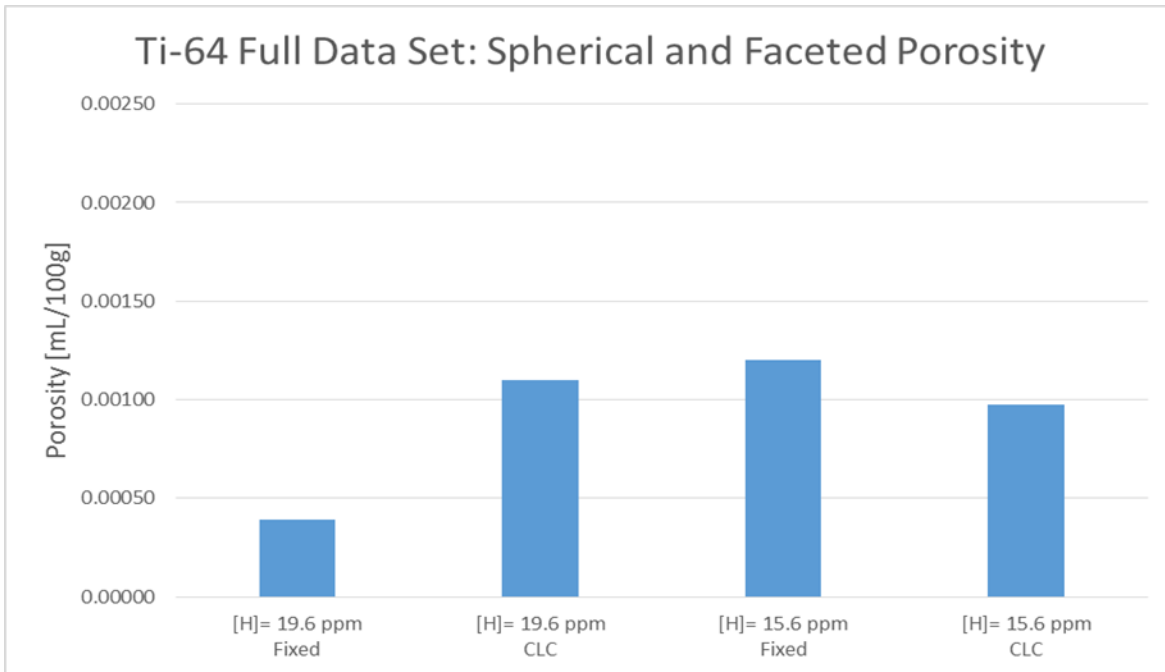
Figure 23: Plot of total porosity in Ti-6Al-4V samples for each combination of hydrogen contamination and process setting
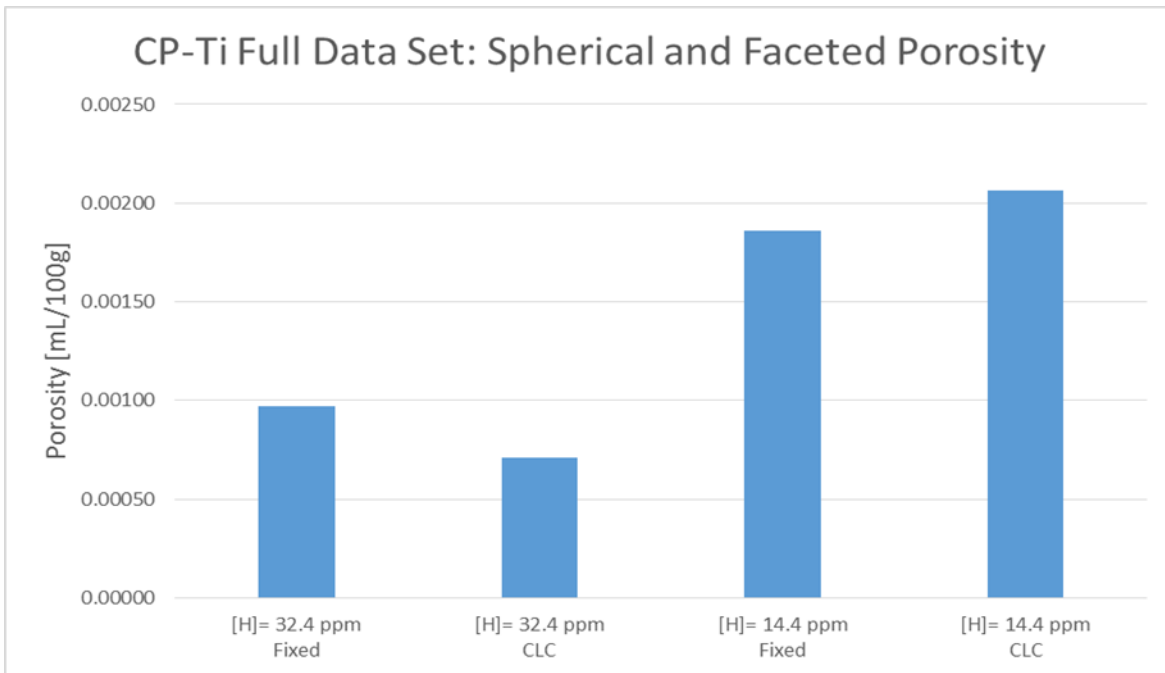
Figure 24: Plot of total porosity in CP-Ti samples for each combination of hydrogen contamination and process setting
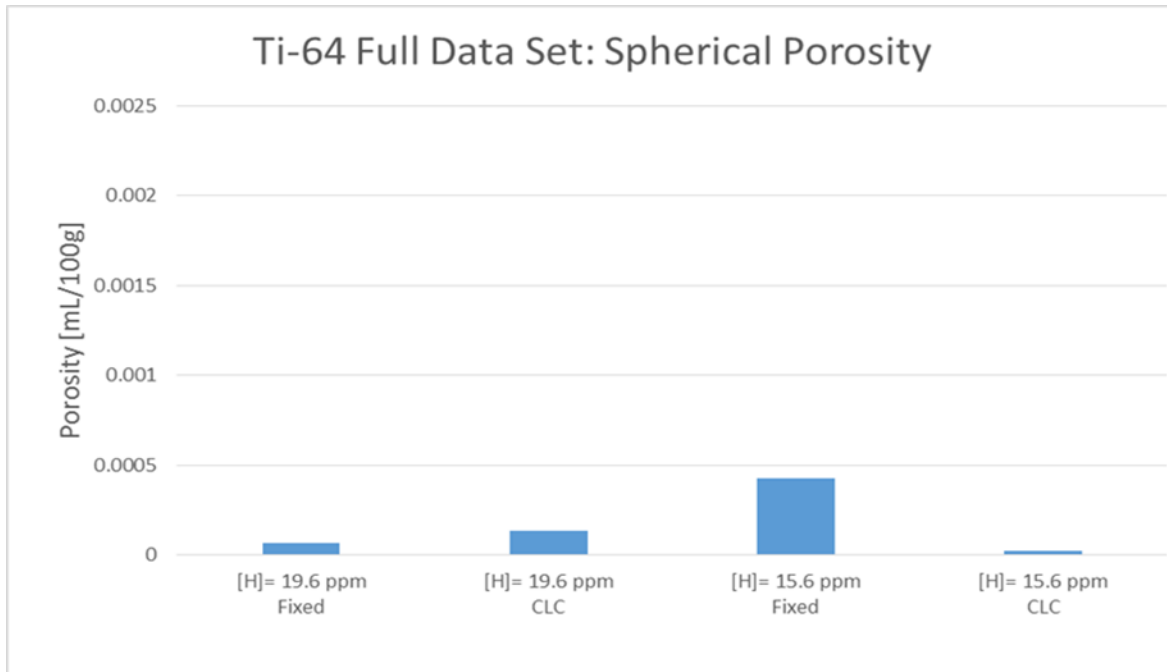
Figure 25: Plot of spherical porosity in Ti-6Al-4V samples for each combination of hydrogen contamination and process setting
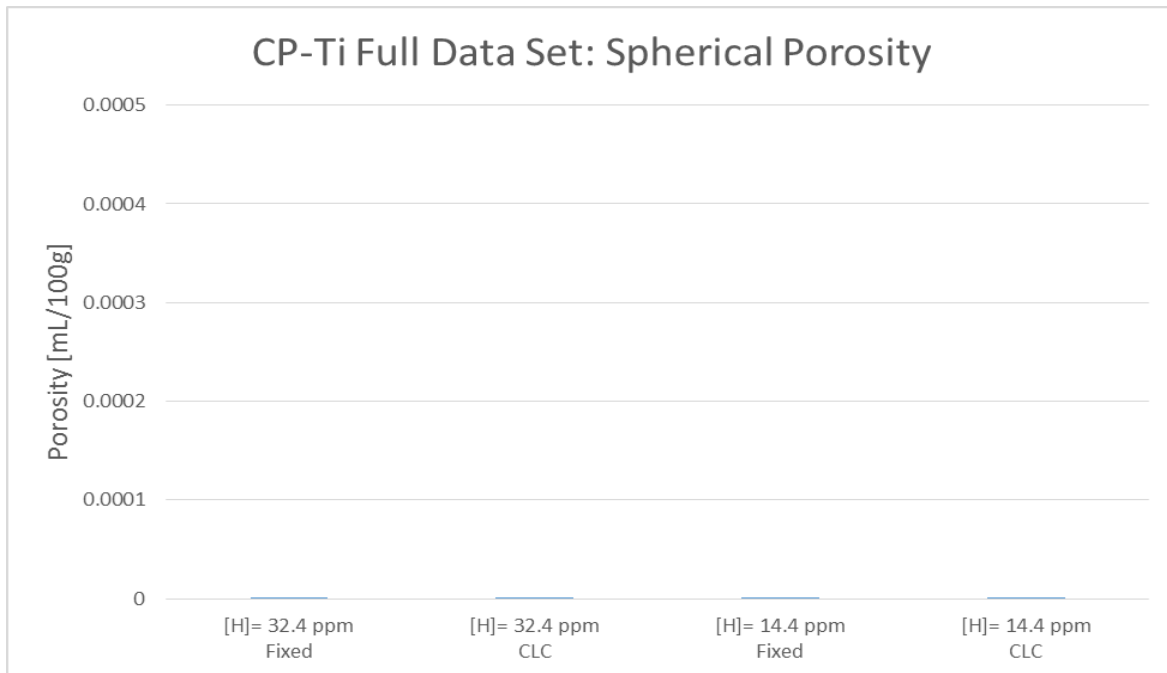
Figure 26: Plot of spherical porosity in CP-Ti samples for each combination of hydrogen contamination and process setting
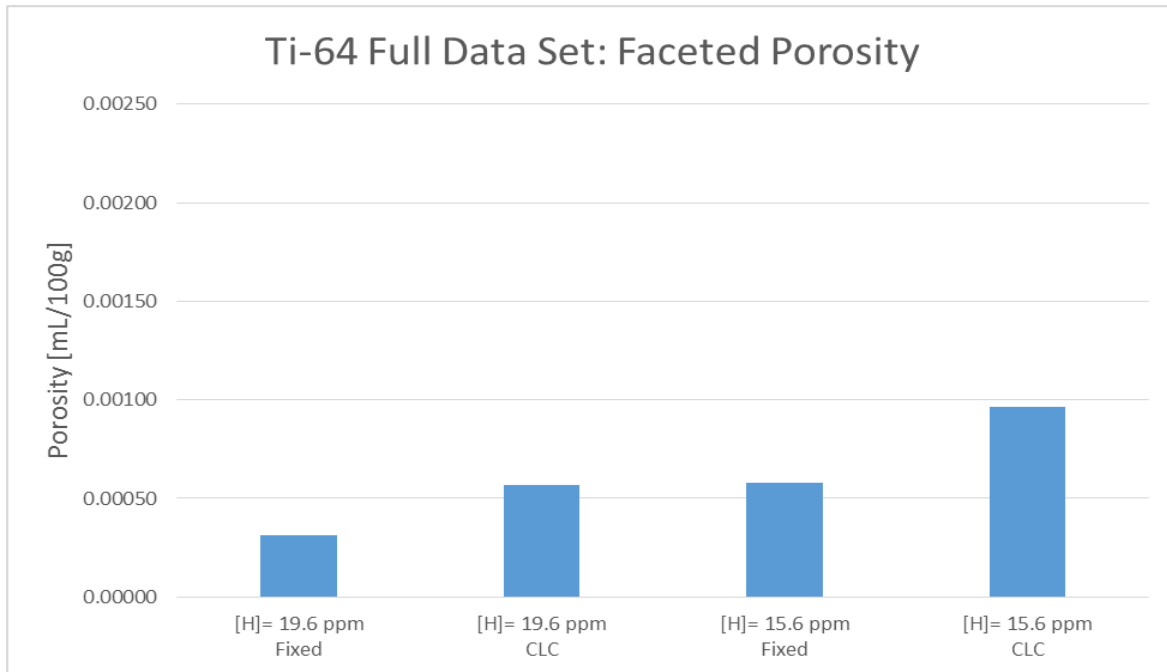
Figure 27: Plot of spherical porosity in Ti-6Al-4V samples for each combination of hydrogen contamination and process setting
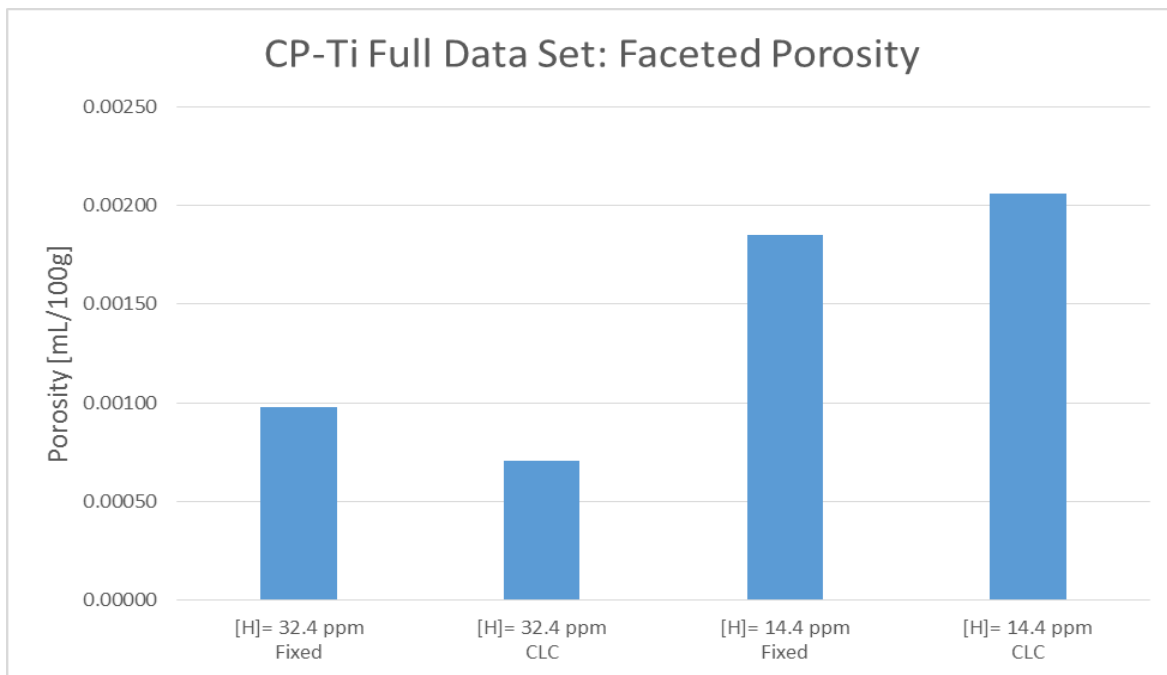
Figure 28: Plot of spherical porosity in CP-Ti samples for each combination of hydrogen contamination and process setting

Analysis of Variance

An analysis of variance (ANOVA) was employed to further understand the relationship between the experimental variables and the degree of porosity. This test was used to determine which independent variables have a statistically significant effect on the different pore characteristics. The pore characteristics evaluated during the OM analysis allows the porosity data to be tested in the ANOVA based on pore size, morphology, and location. The independent variables from the initial hypothesis (aluminum content, wire quality, and process parameters) were evaluated and found to have different effects at different locations in the build. Additionally, data from other potential independent variables, including surface sulfur and fluorine content, bulk nitrogen content, starting vacuum levels, and change in vacuum levels. All independent variables, or factors, tested were evaluated and removed based on an F-Test with $\alpha = 0.10$. Finally, transformations were applied to the data to maintain the ANOVA model assumptions of a normal, independent distribution with a mean of zero and a standard deviation of σ^2.

ANOVA Results

At the interface, there is only a significant effect from the aluminum content, where the Ti-6Al-4V samples (higher aluminum content) produced more porosity compared to CP-Ti. There is a significant effect from the aluminum content and the hydrogen content, or wire contamination, on the porosity in the deposit region of the samples. The effect from the aluminum content is opposite of its effect at the interface, producing more pores in CP-Ti deposits compared to Ti-6Al-4V. The effect from hydrogen content shows an increase in the level of porosity with a decrease of hydrogen content in the

wires used. This is not the effect that was expected in the initial hypothesis but agrees with the results

from OM and stereology.

SEM and EDS

SEM and EDS characterization techniques were used to evaluate the identified spherical porosity

on the surface of the sample. Micrographs of the pores and their inner surfaces were obtained from SEM,

then EDS was used to determine the chemical composition near the pore-metal interface. The inner

surface roughness of the pore was evaluated to check for spherical pores with a ripped inner surface,

thought to be formed from vaporized aluminum [18]. Since aluminum vaporization is likely occurring

during this process, the chemical composition near the interface may show differences in aluminum

content. The SEM micrographs of the pores in Figure 29a and 30a were typical of all the pores

evaluated, containing a smooth inner surface. The rough surface on the pore in Figure 30a is likely due to

material smearing during the grinding stage of metallography. The EDS chemical composition maps are

listed in Figure 29 and 30, with the corresponding SEM micrographs. In Figure 29a there appears to be a

higher count of aluminum on the inner surface of the pore, compared to the surrounding metal. It is

possible that this is the result of an edge effect present due to the angle of the detector and depth of the

pore. This may be possible, but if so, there should be a similar effect observed for titanium, which

appears to have less counts inside the pore. The higher aluminum content on the inner pore surface could

be a result of aluminum vapor becoming trapped upon solidification and then condensing to the inner

surface of the pore.
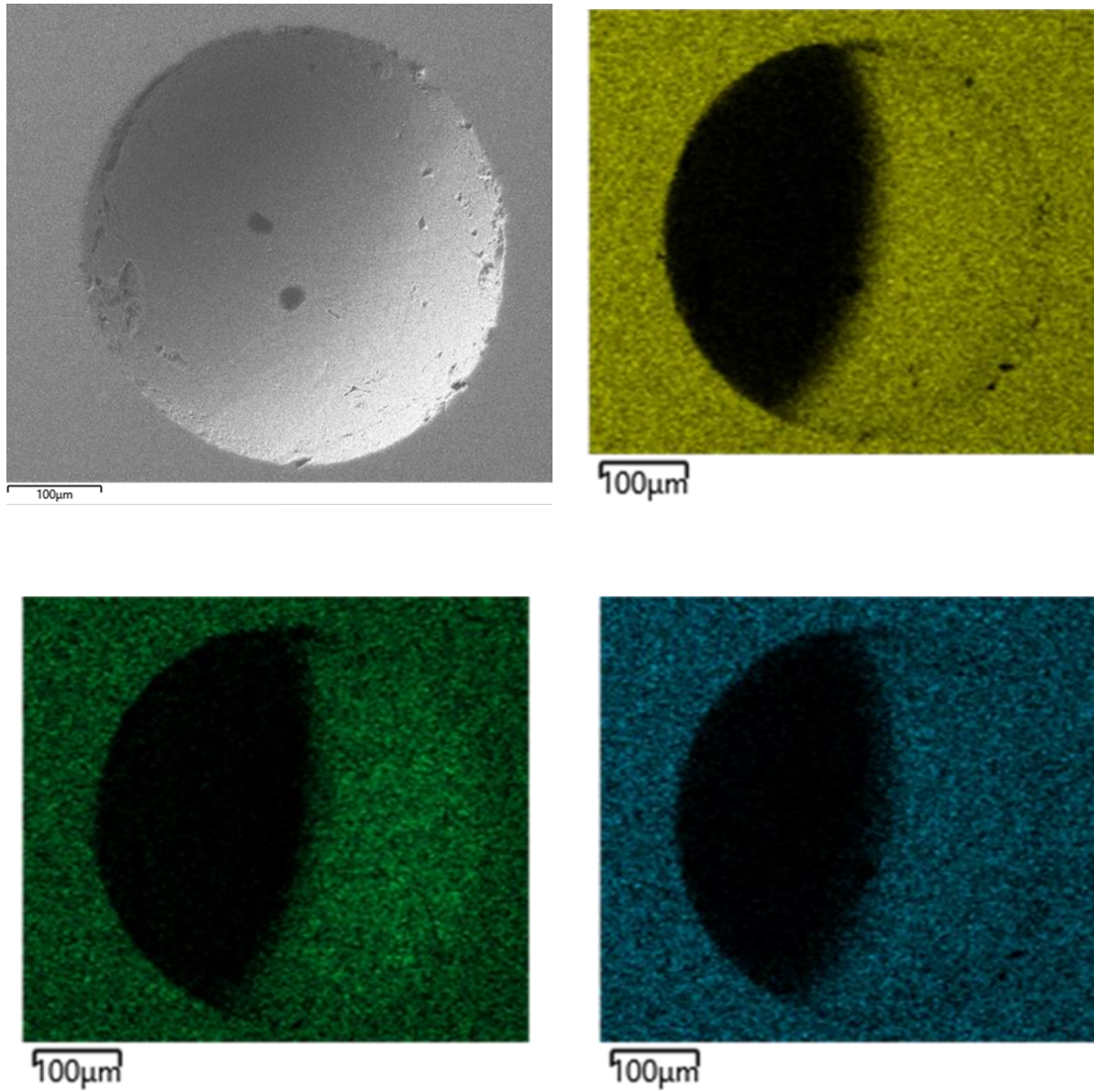
Figure 29: Sample 1C: Ti-6Al-4V with low (15.6 ppm) H content SEM micrograph (a), and chemical composition map of Ti (b), Al (c), and V (d).
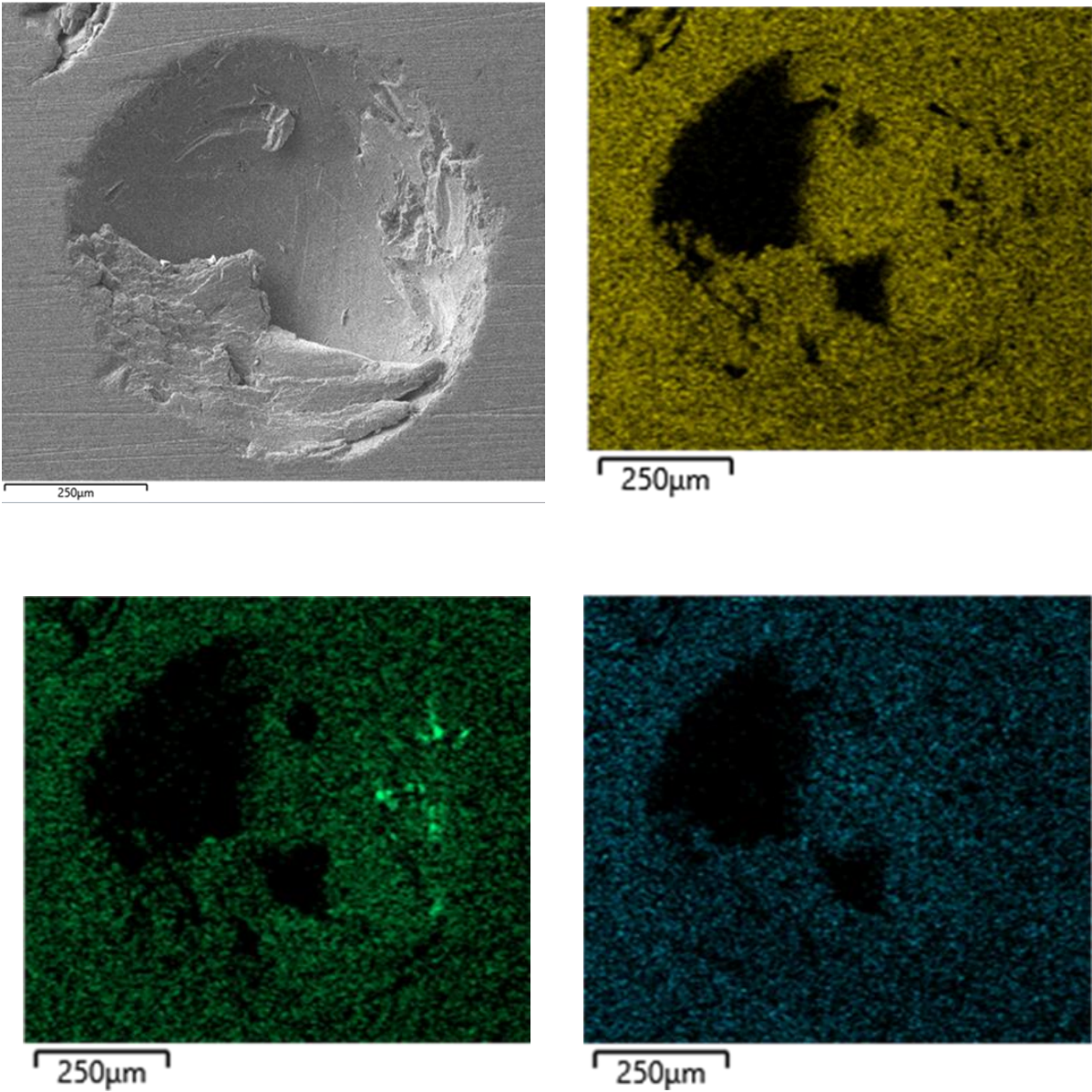
Figure 30: Sample 1C: Ti-6Al-4V with low (15.6 ppm) H content SEM micrograph (a), and chemical composition map of Ti (b), Al (c), and V (d).

SEM and EDS Summary

The inner surface roughness and chemical composition at the gas-metal interface of the pore was evaluated using SEM and EDS. SEM micrographs showed that all pores had a smooth inner surface, and no "ripped" or rough surfaces were identified. The presence of pores with a rough inner surface was expected as a result of vaporized aluminum. Although there were no spherical pores with a rough inner surface, it is still possible that vaporized aluminum may cause spherical porosity with a smooth surface. It should be noted that the pore in Figure 30 has a smooth inner surface, and the rough features are likely a result of smearing during grinding. This was of interest due to the clusters of aluminum observed in the rough features of the pore, which could be a result of aluminum vaporization during processing. It is more likely that the clusters of aluminum are counts of residual alumina, which was used during polishing. The higher aluminum content on the inner pore surface could be a result of aluminum vapor becoming trapped upon solidification and then condensing to the inner surface of the pore. It is possible that this is the result of an edge effect present due to the angle of the detector and depth of the pore. If this were the case, there should be a similar effect observed for titanium, which appears to have less counts inside the pore.

X-ray Computed Tomography

X-ray Computed Tomography (X-ray CT) was used to identify and evaluate internal features and porosity. This characterization technique can provide information on the 3D location and distribution of porosity, pore size, and pore morphology. The effectiveness of this analysis is limited by the feature

resolution, which is a function of voxel size. Two sections were scanned with a 20 µm voxel size,

corresponding to a feature resolution of approximately 60 µm. Sample 1A (Ti-6Al-4V, low hydrogen,

and fixed process settings) and Sample 5C (Ti-6Al-4V, high hydrogen, and fixed process settings) were

chosen at random to evaluate using X-ray CT. Differences in pore location, distribution, and size were

observed between both samples.

Figure 31: Sample 1A X-ray CT scan of top of deposit
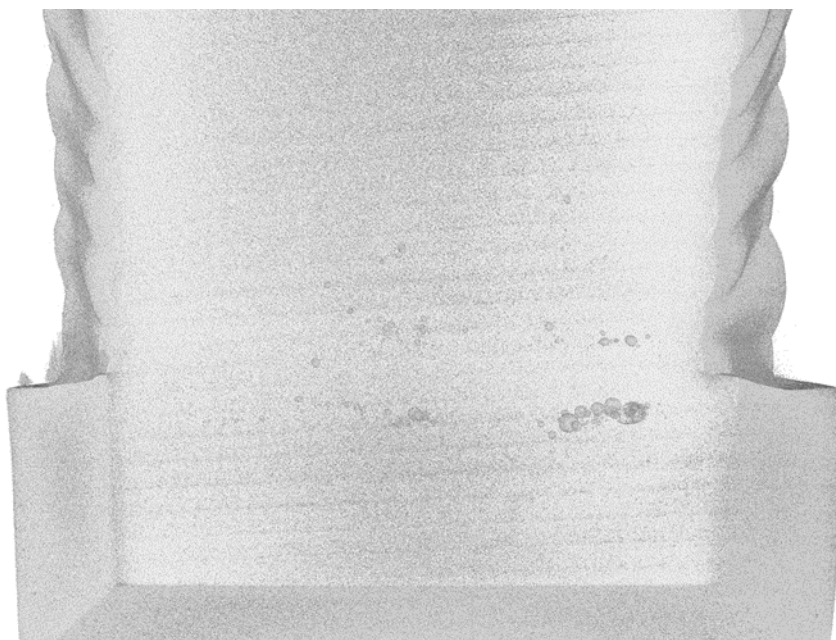
Figure 32: Sample 1A X-ray CT scan of interface region

X-Ray CT Results

Generated images from the X-ray CT scans of Sample 1A can be seen in Figure 31 and 32.

Figure 31 contains the top of the deposit where a high density large spherical pores can be identified.

One pore is significantly larger than the rest and appears to have a cluster of smaller spherical pores

following the large spheres float path. The interface of Sample 1A is shown in Figure 32, which has a

high density of pores, similar to the top of the sample. Additionally, it is clear that the porosity formed in

a layered pattern, at the bottom of the first few layers in the interface region. These scans show a high

density of pores at the interface and at the top of the sample, and minimal porosity in the middle of the

sample.

Figures 33 and 34 are images of the top and interface of Sample 5C, generated from X-ray CT

scans. Spherical pores are observed at the top of the sample in Figure 33, but with a lower distribution

density than the pores observed at the top of Sample 1A. Also, unlike Sample 1A, pores are distributed

throughout the entire height of the sample. The distribution of pores in Sample 5C appears to be more

uniform with an increase in density with increasing height. There are few pores located at the interface

making it difficult to determine if the pores formed in layers like Sample 1A.
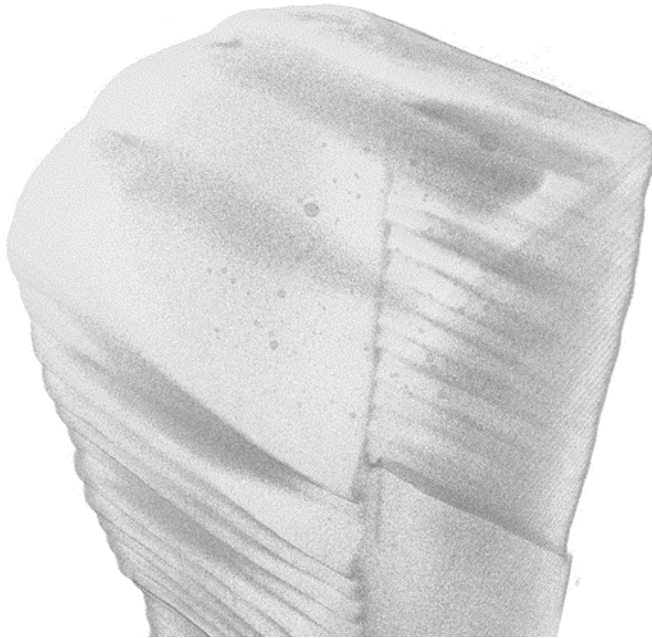
Figure 33: Sample 5C X-ray CT scan of top of deposit
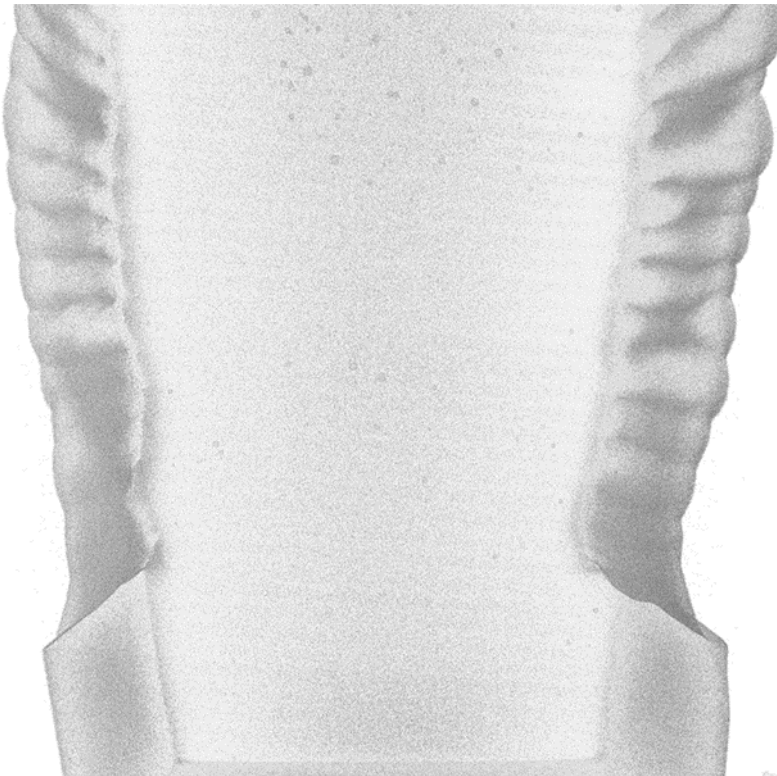
Figure 34: Sample 5C X-ray-CT scan of interface and middle of deposit.

Summary of X-ray CT Results

Sample 1A and 5C were evaluated using X-ray CT to identify and evaluate internal porosity. Both samples were found to have different pore sizes, locations, and distribution. Also, it is important to note that no faceted pores were observed in either of the samples, meaning the observed faceted pores are not voids in the material in the as-deposited condition. This indicates that the faceted pores may be a result of material being removed during grinding or polishing.

Both samples had noticeable differences in their distribution of porosity. Sample 1A had a majority of its porosity in clusters at the top of the deposit or layered at the interface and only a few counts observed in the middle of the sample. Sample 5C had a more uniform distribution of porosity, but still appeared to have an increasing amount of porosity as sample height increases. The only controlled difference between these two samples is that Sample 1A has lower (15.6 ppm) hydrogen content compared to Sample 5C (19.6 ppm). Although this is a small difference, the additional hydrogen in Sample 5C may supply enough hydrogen for the pores to grow, making them more likely to float through the melt and escape.

Chapter 5: Theoretical Model for Pore Formation Mechanisms

Pore Formation Mechanisms

It is important to understand the mechanisms that cause pore formation and the factors that will influence those mechanisms. Formation of pores can be split up into three different mechanisms: nucleation, growth, and rise or flow in the melt pool [7]. The solubility of hydrogen in titanium suggests that hydrogen is rejected from the melt upon cooling to the solidification temperature [7,8,22]. Given this, it is expected that porosity formation is most likely to occur during solidification. If liquid titanium is supersaturated with hydrogen, a bubble will nucleate once a sufficient amount of hydrogen is rejected. This will establish a hydrogen concentration gradient, causing hydrogen to diffuse from a hydrogen rich region towards the bubble. If there is sufficient time before solidification, the bubble will begin to grow and float in the melt pool, giving it the potential for escape. These mechanisms are visually represented in Figure 35 and are explained in further detail in the upcoming sections.

Initial- Liquid titanium supersaturated with hydrogen

Hydrogen solubility decreases with temperature

Jump in solubility at T_m rejects H upon solidification

Nucleation- Dynamics of nucleation

At high supersaturation and decreasing solubility, bubble nucleation can occur

Nucleation is driven by surface tension, melt temperature, and inertial forces

Growth- Driving force for pore growth

Once the pore nucleates, a concentration gradient is formed due to the reduction of hydrogen in the liquid metal surrounding the pore

Gradient drives diffusion of hydrogen towards depleted region around the pore

Rise- Bubble flow in melt pool due to buoyancy effects

riven by buoyancy, liquid properties, and fluid flow within the melt pool

Bubbles may escape the melt pool if sufficient time and energy are available

Figure 35: Summary of pore formation mechanisms [7,22]

Nucleation

Nucleation can occur homogeneously within the liquid, or heterogeneously on a surface or interface. In both types of nucleation, an energy barrier must be overcome to form a new interface in order for nucleation to occur. The energy barrier (ΔG^*) to form a critically sized cluster (r^*) and rate of impingement (g^*) to make the nucleus free-growing are required to determine the nucleation rate (J). Homogeneous nucleation is simplified version of heterogeneous nucleation, due to the absence of a nucleating surface, and will be used to initially evaluate the nucleation rate [26].

The homogeneous nucleation rate can be calculated by starting with the equation for total free energy of the system. This is represented by Equation 11, where r is the bubble radius, γ is the surface tension, and ΔG_V is the free energy from the change in volume.

$$\Delta G_{tot} = 4\pi r^2 \gamma - \frac{4}{3}\pi r^3 \Delta G_V \qquad (11)$$

The critical radius (r^*) of the nucleus can be determined by differentiating ΔG_{tot} with respect to r and setting equal to zero.

$$r^* = \frac{2\gamma}{\Delta G_V} \qquad (12)$$

The critical radius can be substituted for r in Equation 11 to determine the free energy required to create a critically sized nucleus.

$$\Delta G^* = \frac{16\pi\gamma^3}{3\Delta G_V^2} \qquad (13)$$

With the height of the energy barrier known, the number of critically sized nuclei formed (n^*) is calculated by Equation 14. A is a constant, k is Boltzmann's constant, and T is in Kelvin.

$$n^* = A \exp(-\frac{\Delta G^*}{kT}) \qquad\qquad (14)$$

The next step in calculating the nucleation rate is determining the rate at which a critically sized nuclei

obtains one more unit, making it a free-growing nucleus. This can be expressed by the Hertz-Knudsen

equation for the rate of impingement:

$$g^* = \frac{pO}{\sqrt{2\pi mkT}} \qquad\qquad (15)$$

where p is the ambient pressure and O is the surface area. Now, the overall homogeneous nucleation rate

(J) can be expressed as:

$$J_{ho} = n^* g^* = C \exp(-\frac{\Delta G^*}{kT}) = C \exp(-\frac{16\pi\gamma^3}{3\Delta G_V^2 kT}) \qquad\qquad (16)$$
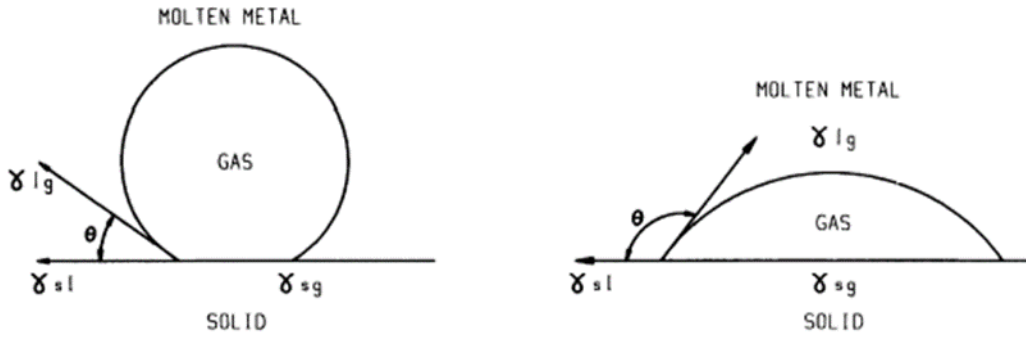
Figure 36: Representation of heterogeneous nucleation with different contact angles
reproduced from [26]

In order for heterogeneous nucleation to occur, additional material in the system is considered,

acting as a catalyst for the phase transition. When a surface or interface is present, the energy barrier to

nucleate will decrease due to the lower volume required to nucleate a critically sized bubble [26]. The

fraction of volume required is a function of the contact angle, θ, between the solid and the gas, as shown

in Figure 36. The function for bubbles is represented as:

$$\Phi(\theta) = \frac{(1+\cos\theta)^2(2-\cos\theta)}{4} \qquad (17)$$

Now, the heterogeneous nucleation rate can be written in terms of the homogeneous nucleation rate and

the function of contact angle:

$$J_{he} = C'\exp(-\frac{16\pi\gamma^3\Phi(\theta)}{3\Delta G_V^2 kT}) \qquad (18)$$

Growth

The growth of pores is related to the degree of supersaturation, inertia of the liquid metal, surface

tension, ambient pressure, and gas content of the metal. Once a critical bubble is formed, it is expected

to grow, unless the nucleation stage depleted the supersaturated system [26]. The growth rate of a pore

is,

$$\frac{dr}{dt} = \frac{2(P_g - P_{atm} - P_b - P_h)(r_1 - r_0) - 2\gamma}{3\eta} \qquad (19)$$

where P_g is the partial pressure of the soluble gas, P_{atm} is the atmospheric pressure, P_b is capillary pressure

due to the curvature of a pore, and P_h is the hydrostatic pressure from the depth in the liquid metal [26].

Growth rate is affected by the speed in which material can be transported across the interface. The final

radius or size of the pore depends on the amount of time during which the metal is in the liquid state.

Given this, the highest growth rate is expected to occur when a gas species has a high diffusivity in a

liquid metal for an extended amount of time [26].

Rise and Flow in the Melt

After the bubble nucleation stage and during growth, rise in the liquid metal begins due to buoyancy forces [26]. Stokes Law from the Navier-Stokes equation can be used to describe the terminal rise velocity of a bubble as:

$$V = \frac{2gr^2\Delta\rho}{9\eta} \qquad (20)$$

where g is the acceleration due to gravity, r is radius of the bubble, $\Delta\rho$ is the difference in density between the gas phase and the liquid metal, and η is the viscosity. It is important to note that the Stokes Law solution assumes the size of the bubble remains constant during rise. This does not account for the effect that as the bubble rises, it will continue to grow due to decreasing hydrostatic pressure. In addition to buoyancy forces, Marangoni flow and electrostatic interactions may affect the flow of the bubble in the liquid metal. Since both effects require the presence of a surface, these interactions may have a greater effect on bubble flow during the earlier stages of rise. Also, as the bubble continues to rise and grow, the buoyancy forces will begin to overpower the effects from Marangoni and electrostatic interactions. Given a sufficient supersaturation and time in liquid metal, pores may nucleate, grow, rise, and eventually escape. In order for this to occur, enough free energy must be available for the pore to create a new surface upon expulsion from the melt [26].

Liquid Properties of Ti-6Al-4V and CP-Ti

Surface Tension (Ti-6Al-4V v CP-Ti)

Surface tension is a measure of the excess surface energy due to a net inward force on the surface atoms. The atoms in the bulk of the liquid are bonded in all directions, resulting in a net 0 force. Atoms on the surface of the material only have bonds inward, giving rise to the net inward force at the surface [27-29]. In order to decrease the free energy of the system, liquids will attempt to decrease their surface area to achieve the smallest possible surface area to volume ratio. Surface tension plays a role in the nucleation, growth, and escape stages of pore formation. A material with a higher surface tension is expected to have a lower bubble nucleation rate, growth rate, and escape probability, based on Equations 16 and 18.

The surface tension for Ti-6Al-4V and CP-Ti was calculated using empirical results from Zhou et al. over a range of temperatures near the solidification temperature [27,28]. The data from this experiment was collected using the oscillating drop method over the temperature range of 1700-2300 K for Ti-6Al-4V and 1802-2188 K for CP-Ti. The following equations were used to calculate the surface tension of Ti-6Al-4V and CP-Ti as a function of temperature, and the results are plotted in Figure 37. As you can see from the results, Ti-6Al-4V has a lower surface tension compared to CP-Ti and it can be said that the addition of aluminum to pure titanium decreases the surface tension. [27,28]

$$\text{CP-Ti: } \sigma[\tfrac{N}{m}] = 1.64 - 2.38 \times 10^{-4} * (T - 1943) \qquad (21)$$

$$\text{Ti-6Al-4V: } \sigma[\tfrac{N}{m}] = 1.38 - 3.13 \times 10^{-4} * (T - 1933) \qquad (22)$$
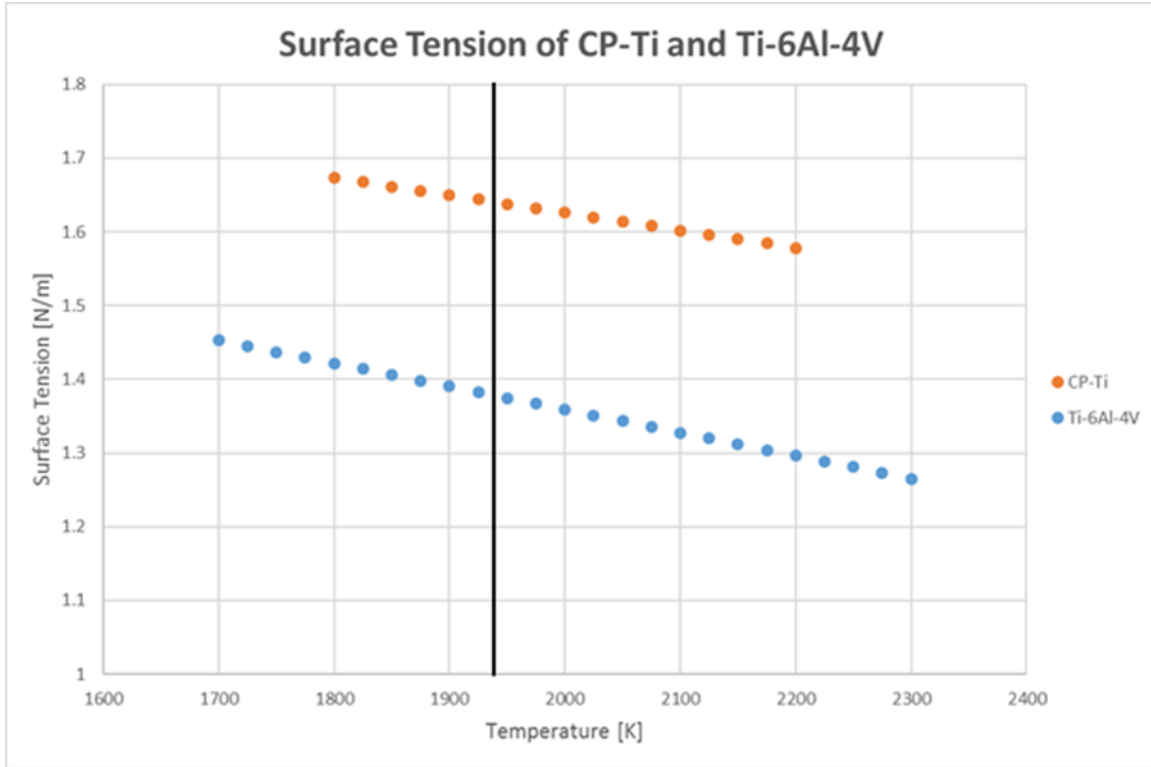
Figure 37: Plot of Ti-6Al-4V and CP-Ti surface tension as a function of temperature

Viscosity

Viscosity is a measure of a materials resistance to fluid flow and plays a role in bubble growth and rise in a liquid melt. A material with a greater viscosity is expected to have a lower bubble growth rate, and float velocity in the melt. The viscosity for Ti-6Al-4V and CP-Ti was calculated using empirical results from Zhou et al. and Egry et al over a temperature range near the solidification temperature. The following equations were used to calculate the viscosity of Ti-6Al-4V and CP-Ti as a function of temperature, and the results are plotted in Figure 38. As you can see, the results are similar to the surface tension results, where Ti-6Al-4V has a lower viscosity than CP-Ti due to the additional aluminum content in the alloy. [27,28]

$$\text{CP-Ti: } \eta[mPa * s] = \frac{16}{15}\sqrt{\frac{M_{CP-Ti}}{kT}}\sigma \qquad (23)$$

$$\text{Ti-6Al-4V: } \eta[mPa * s] = \frac{16}{15}\sqrt{\frac{M_{Ti-64}}{kT}}\sigma \qquad (24)$$
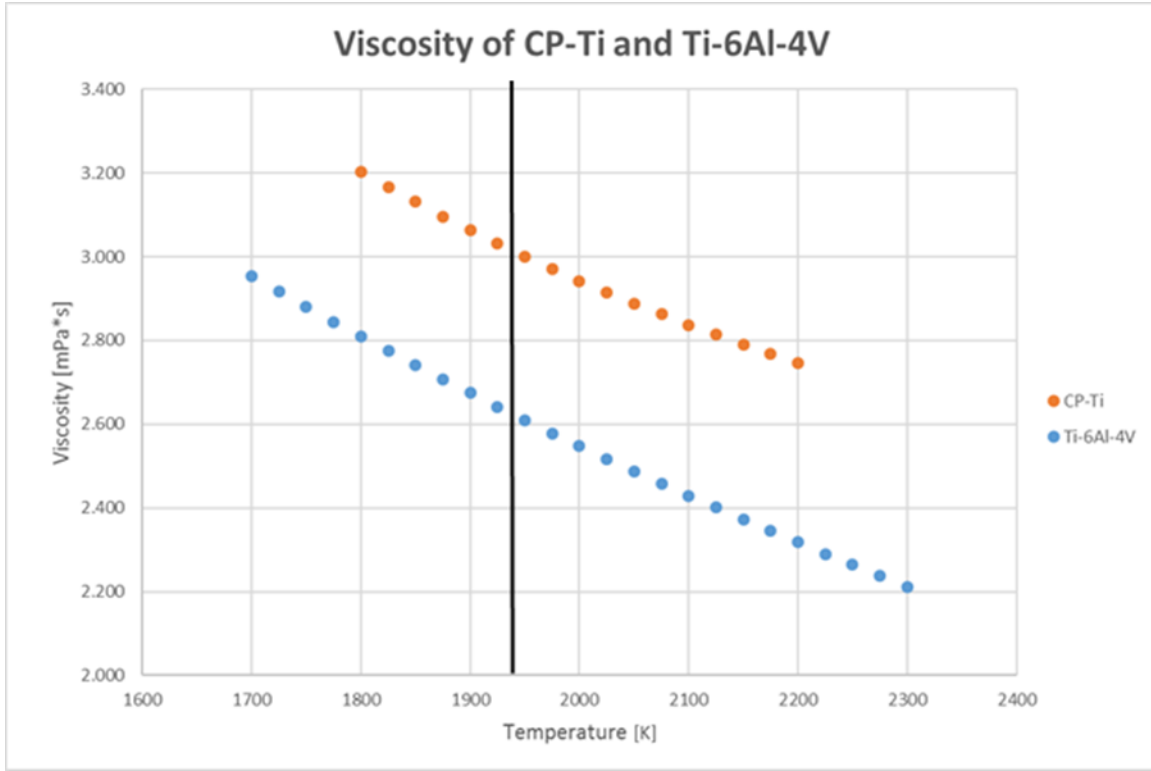
Figure 38: Plot of Ti-6Al-4V viscosity as a function of temperature

Density

The density of Ti-6Al-4V and CP-Ti was calculated using the following equations [27,29]:

$$\text{Ti-6Al-4V: } \rho\left[\frac{g}{cm^3}\right] = 4.12 - 2.54 \times 10^{-4} * (T - 1933) \qquad (25)$$

$$\text{CP-Ti: } \rho\left[\frac{g}{cm^3}\right] = 4.13 - 4.29 \times 10^{-4} * (T - 1943) \qquad (26)$$

Both equations have a similar density at the melting temperature, but different temperature coefficients.

Figure 39 shows the change in density with temperature for Ti-6Al-4V and CP-Ti, where CP-Ti has the

greater liquid density and Ti-6Al-4V has the greater solid density. The higher liquid density of CP-Ti

will promote faster bubble rise due to a greater difference in density between the liquid metal and the gas

bubble.
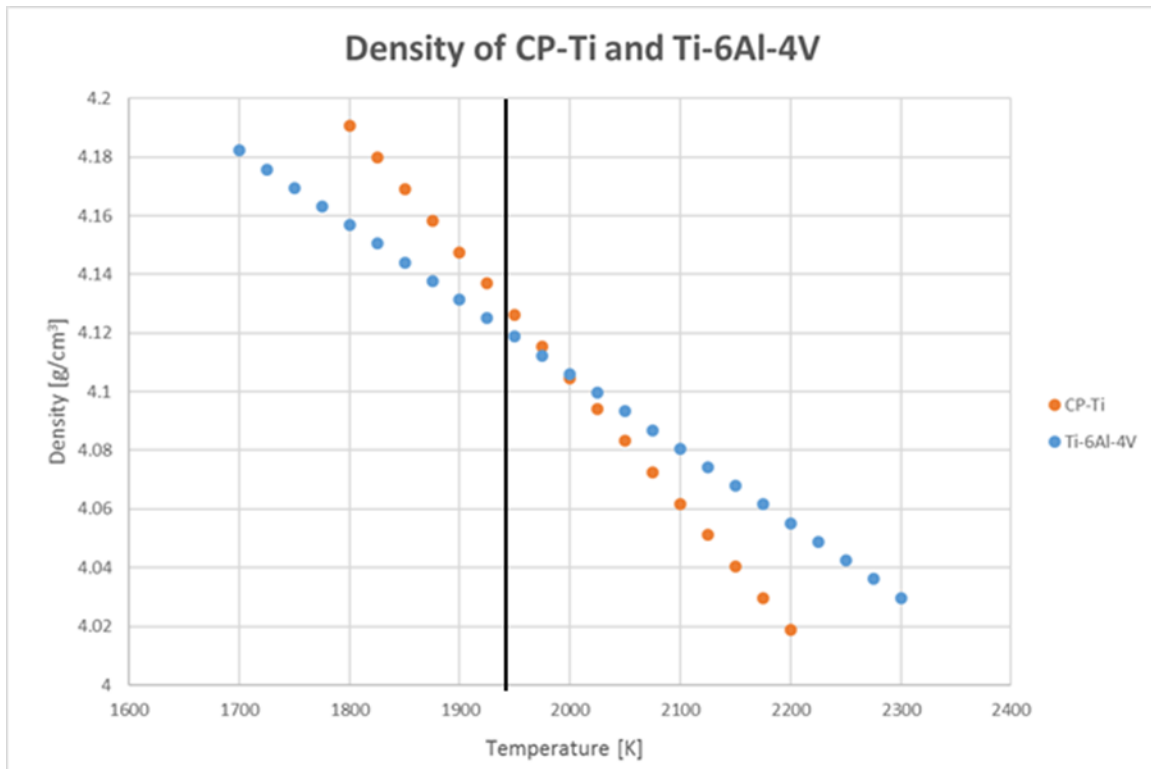
Figure 39: Plot of Ti-6Al-4V and CP-Ti density as a function of temperature

Nucleation Rate

The calculated values for surface tension, viscosity, and density can be applied to the equations

from the pore formation mechanisms to determine the differences in porosity between Ti-6Al-4V and CP-

Ti. The nucleation rate was determined using the classical nucleation rate equation:

$$J = C\exp\left(\frac{-16\pi\sigma^3\Omega^2}{3k^3T^3\ln^2\left(\frac{p}{p_o}\right)}\right) \qquad\qquad (27)$$

where σ is the surface tension, Ω is the energy exchange coefficient, k is Boltzmann's constant, T is in K, and P is the normalized pressure of the bubble. Using Equation 27, the effect of aluminum content on surface tension can be determined by comparing the nucleation rates of the two alloys. These results are shown in Figure 40. Ti-6Al-4V is expected to have a greater nucleation rate than CP-Ti. This can be further supported by the higher surface tension material (CP-Ti) will require more energy to create a new surface and therefore is expected to have a lower nucleation rate.
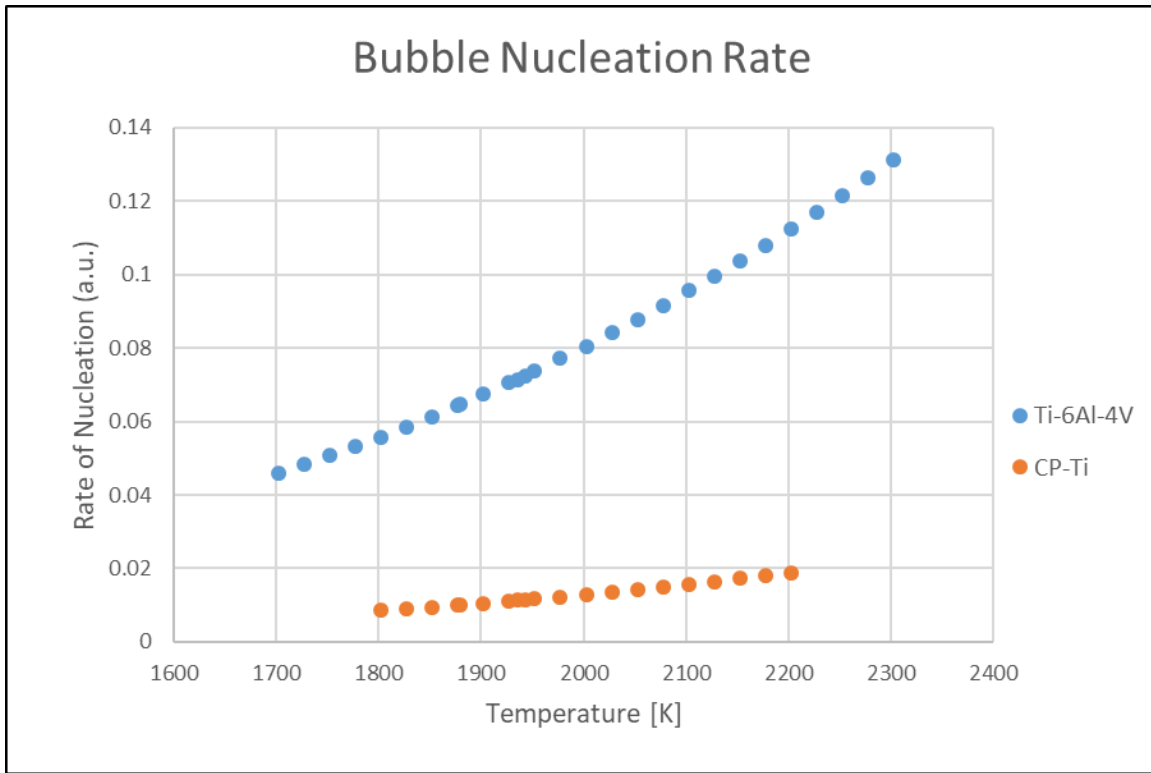
Figure 40: Plot of Ti-6Al-4V and CP-Ti nucleation rate as a function of temperature

Growth Rate

Similarly, the calculated liquid metal properties can be applied to the growth rate equation as well. In the growth rate equation (Equation 19), surface tension and viscosity are identified as important liquid metal properties that will change with varying alloying content. The results for the bubble growth rate between the two alloys is reported in Figure 41, where Ti-6Al-4V is expected to have a higher bubble growth rate than CP-Ti.
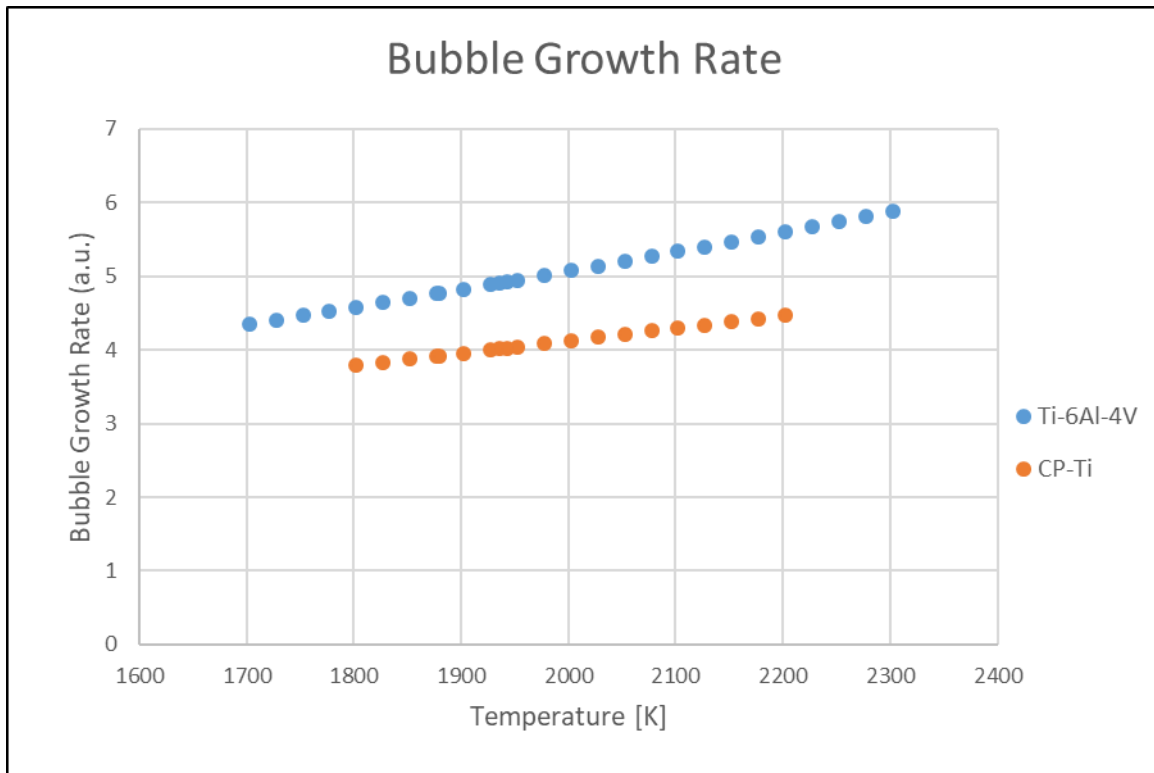
Figure 41: Plot of Ti-6Al-4V growth rate as a function of temperature

Summary of Pore Formation Mechanisms in CP-Ti and Ti-6Al-4V

There are three main stages of porosity formation which are influenced by the liquid metal properties of the material of interest. In the case of this experiment, the addition of aluminum to titanium alters the liquid properties and the extent of the pore formation mechanisms of Ti-6Al-4V. Adding aluminum to titanium decreases the surface tension and viscosity at the solidification temperature, while the density at this temperature remains constant. Above the melting temperature, in the liquid phase, CP-Ti has a greater density than Ti-6Al-4V. When these are applied to the pore formation mechanism equations, it was found that Ti-6Al-4V is expected to have a greater bubble nucleation and growth rate due to the decrease in surface tension and viscosity. Bubble rise in Ti-6Al-4V is expected to increase due to the greater difference in density between liquid Ti-6Al-4V and the gas bubble. In addition, it is important to note that the larger pores in Ti-6Al-4V (from the faster growth rate) will also provide an increase in float velocity. In addition to this, there are also Marangoni flow and electrostatic interactions that will influence the bubble flow in the liquid, making it even more difficult to determine relative float velocities.

Hydrogen in Titanium and Alloys

Hydrogen Solubility in Liquid Titanium

Unlike other materials, such as aluminum or steel, the solubility of hydrogen in titanium decreases with increasing temperature [30-33]. There is a local max in the hydrogen solubility at the solidification temperature with a rapid drop in solubility upon solidification. This jump in solubility may

partition some hydrogen and cause it to diffuse to lower temperatures, until it reaches the β transus. The magnitude of the jump in solubility is defined by the ratio of the equilibrium constants for the gas species in liquid and solid metal. Lakomski et al. derived the following equation to calculate the magnitude in the jump of hydrogen solubility in titanium at the solidification temperature [33]:

$$19.15 * \log\left(\frac{K_{li}}{K_{so}}\right) = -\frac{H_{li} - H_{so}}{T_m} - [S_{li}^o - S_{so}^o] \qquad (27)$$

These features can be seen in Figure 42, which is a plot of hydrogen solubility in pure titanium generated from empirical results. The plot takes the form of the following equation [31]:

$$\ln(C_H^i) = \frac{A}{T} + B + \frac{1}{2}\ln(P_{H_2}) \qquad (28)$$

where A and B are empirically derived and P_{H2} is the partial pressure of hydrogen above the melt.
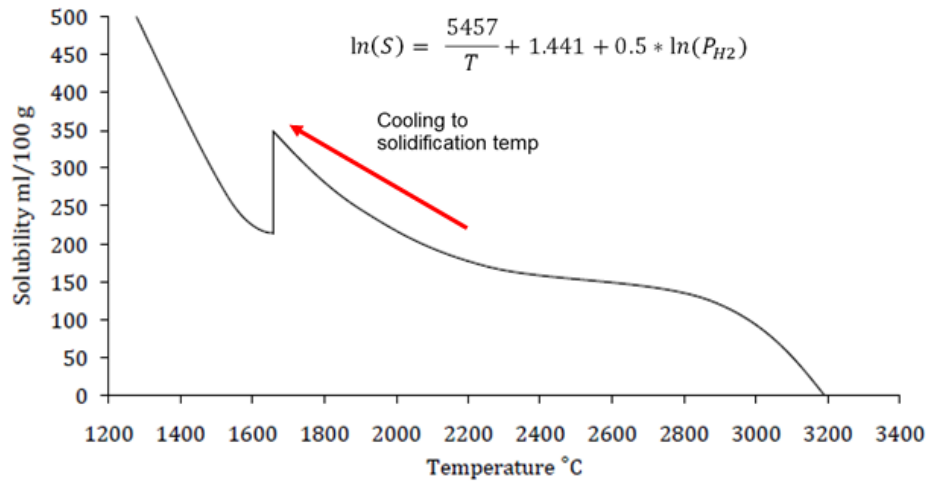
Figure 42: Plot of hydrogen solubility in pure titanium as a function of temperature reproduced from [33]

Calculating Hydrogen Solubility in Alloys

It is difficult to determine hydrogen solubility in alloys through experimentation, so instead it is calculated from thermodynamic data. Typically, hydrogen solubility can be determined using Seivert's Law:

$$C_H = \sqrt{P_{H_2}}\exp(\frac{-\Delta G_M^\theta}{RT}) \qquad (29)$$

where G is the change in molar free energy of hydrogen, P_{H2} is the pressure of hydrogen in Pa, R is the gas constant, and T is in K. This shows the hydrogen solubility in an alloy melt depends on the temperature of the melt and the pressure of hydrogen. To improve this approach, a modified version of Seivert's Law was coupled with a free volume theory which accounted for excess configuration and vibration entropy. Yanqing et al. created a model for calculating the hydrogen solubility in in alloy melts using the modified approach described [31]. The model for hydrogen solubility in an alloy can be written as:

$$lnC_H = \Sigma x_i ln\frac{C_H^i}{\gamma_i} \qquad (30)$$

where C_H^i is the hydrogen solubility in a pure melt, and γ_i is the activity coefficient of i. This equation suggests that only the activity coefficients of the components of the alloy need to be determined to calculate the hydrogen solubility in an alloy melt. An equation to determine the activity coefficients of the component materials was derived by Yanqing et al. and is explained in [31]. With the activity coefficients calculated, the solubility of hydrogen can be calculated using Equation 30. Hydrogen solubility in pure titanium and aluminum was available in literature from previously conducted experiments. There was little-to-no literature available for hydrogen solubility in Ti-6Al-4V so this was

calculated using the method outlined by Yanqing et al. First, an average for the hydrogen solubility for

pure titanium and aluminum was determined based on 3 experimental results for each element and is

reported in Table 10 [30,31,33,34]. It is important to note that the effect of vanadium additions on the

solubility of hydrogen in titanium is negligible compared to the effect from aluminum additions, so

vanadium was not considered in this calculation. [31]

Table 10. Data for hydrogen solubility in pure titanium and aluminum			
Material	**A**	**B**	**Reference**
Ti	5349	4.704	30
Ti	7783	5.779	31
Ti	5457	1.441	33
Ti Average	6196	3.975	Calculated
Al	-6159	6.247	34
Al	-6218	6.264	34
Al	-5953	6.034	34
Al Average	-6175	6.182	Calculated

Figure 43 is a plot of hydrogen solubilities in pure titanium taken from literature, as well as the

calculated average solubilities in titanium and aluminum. The aluminum values taken from literature

were not included in the plot since they all completely overlapped with the average aluminum solubility.

All of the data used for hydrogen solubility in pure titanium agrees well, especially at the solidification

temperature.
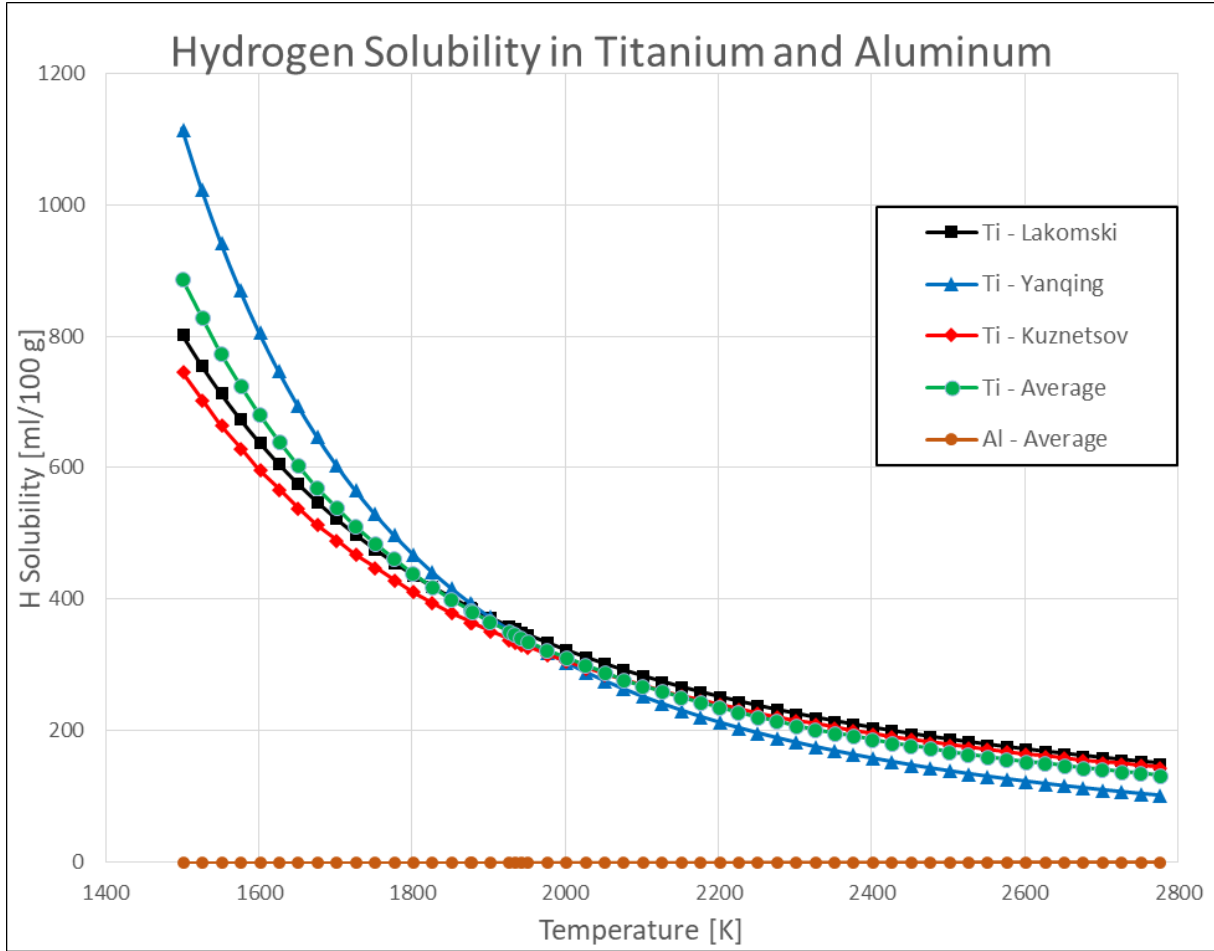
Figure 43: Hydrogen solubility in titanium and aluminum from literature and calculated averages

The average of hydrogen solubility in titanium and aluminum were used as C_H^{Ti} and C_H^{Al} in Equation 30. This, along with the calculated activity coefficients were used to determine the solubility of hydrogen in Ti-6Al-4V. The results from this calculation can be seen in Figure 44, as the line marked Ti-6Al-4V, where it can be compared to the hydrogen solubility in CP-Ti. The lower curves on the plot with the label "Vacuum" consider the hydrogen partial pressure term in Equation 28. Processing in a vacuum causes a decrease in hydrogen pressure above the melt, resulting in a decrease in the hydrogen solubility

of the melt. The "Vacuum" curves are the expected hydrogen solubility limits in the Ti-6Al-4V and CP-titanium samples deposited in this experiment. In both pressure levels, Ti-6Al-4V has a lower hydrogen solubility limit, meaning it will become supersaturated before CP-Ti. In addition to this, Ti-6Al-4V solidifies over a range of temperatures but CP-Ti solidifies at a single temperature. Solidifying over a range of temperatures allows more time for hydrogen diffusion, bubble nucleation, growth, and rise in the melt. CP-Ti's faster solidification time limits hydrogen diffusion may even prevent the bubble nucleation and growth mechanisms. With this, Ti-6Al-4V is expected to have a higher degree of porosity compared to CP-Ti.
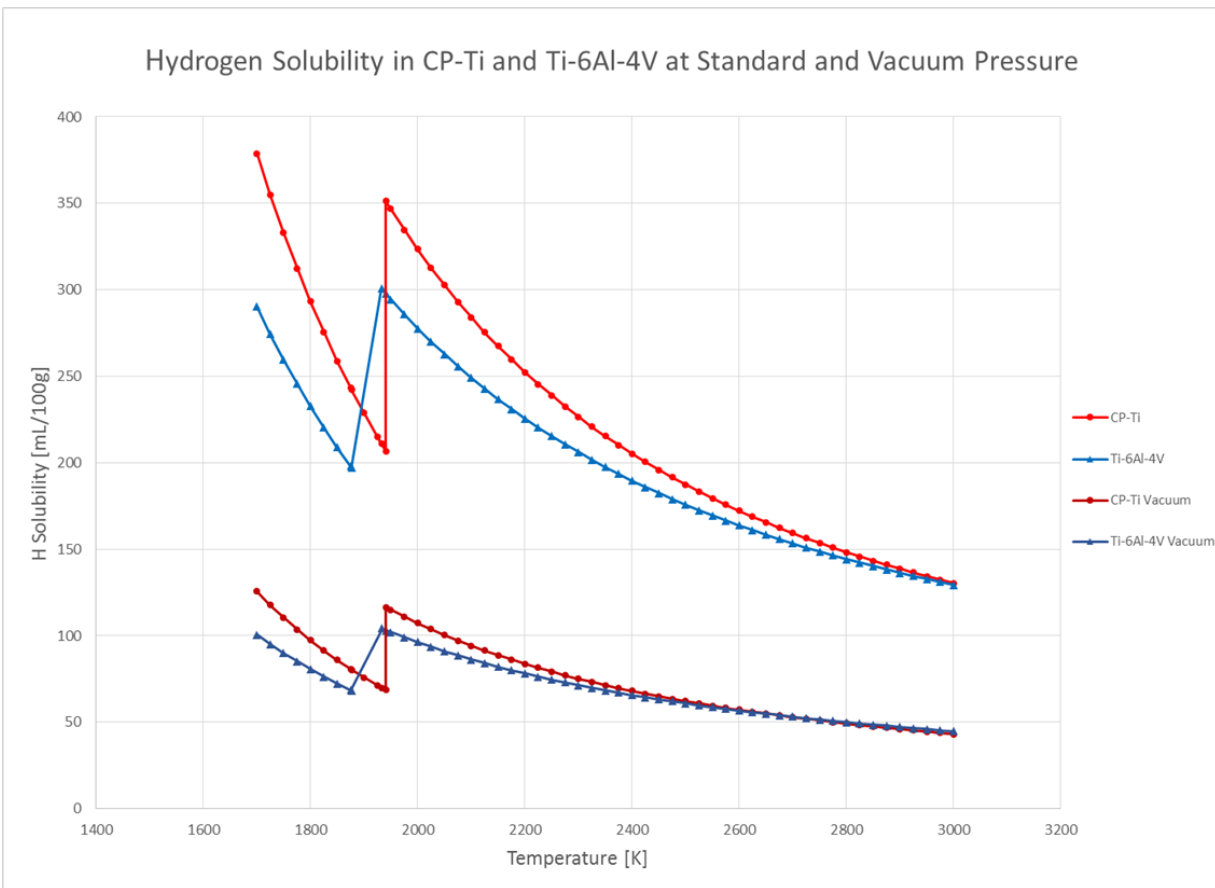
Figure 44: Plot of hydrogen solubility in Ti-6Al-4V and CP-Ti at standard pressure and under high vacuum

Summary of Theoretical Model

A theoretical model for understanding the pore formation mechanisms was established to physically relate to the experimental results. The formation of pores is split into nucleation, growth, and rise mechanisms in the melt pool. These mechanisms were found to be influenced by certain properties of the liquid metal, such as surface tension, viscosity, and density. Furthermore, the aluminum additions in the Ti-6Al-4V alloy affect the liquid properties, decreasing the surface tension and viscosity. The density of both metals was approximately equal near the melting temperature, but Ti-6Al-4V has a higher liquid density than CP-Ti. Due to the difference in liquid metal properties, Ti-6Al-4V is expected to have a higher nucleation and growth rate. If the bubble has sufficient time before solidification, rise will occur, where the higher density of liquid Ti-6Al-4V creates a greater change in pressure between the liquid and the gas, resulting in a faster float velocity. The solubility of hydrogen in titanium is important since it increases upon cooling from the melt, before it reaches a rapid jump in solubility upon solidification. Hydrogen solubility in pure titanium was available in literature, but the hydrogen solubility in Ti-6Al-4V had to be calculated. In addition to this, processing in a vacuum causes a decrease in hydrogen pressure surrounding the melt. A decrease in hydrogen pressure will decrease the solubility limit of hydrogen in titanium, causing it to become supersaturated at significantly lower hydrogen contents. Ti-6Al-4V has a lower hydrogen solubility than CP-Ti, meaning it will become supersaturated first and reject more hydrogen. Additionally, Ti-6Al-4V has a smaller magnitude of jump in solubility over a range of solidification temperatures compared to the larger jump in solubility over a single solidification temperature in CP-Ti. The rapid solidification over a single temperature of CP-Ti may limit the amount of hydrogen that is rejected during solidification, resulting in a low volume of spherical porosity.

Furthermore, any remaining supersaturated hydrogen in CP-Ti will diffuse to form a hydride phase once the titanium has solidified. Recalling that aluminum additions suppress the hydride phase formation due to increased hydrogen solubility in α phase, less hydride phase is expected in Ti-6Al-4V the samples. This could explain the higher amounts of faceted porosity in CP-Ti, since more hydride phase is formed and it is likely that the faceted pores are created by removing hydride phases during grinding. This is further supported by Ti-6Al-4V, where the addition of aluminum is known to suppressed the formation of a hydride phase. This will decrease the formation of a hydride phase, resulting in less faceted porosity in Ti-6Al-4V.

Chapter 6: Discussion of Results

The initial hypothesis evaluated the effect of aluminum content, hydrogen contamination, and process settings on the degree of porosity. Some aluminum is assumed to be vaporized during processing and may form a bubble in the melt and then pore upon solidification. Although the expected ripped inner surface pore was not identified, it is still possible that aluminum vapor may be a cause of porosity. The degree of porosity is expected to increase as the hydrogen contamination increases, but the opposite effect was observed with this data. Also, after analysis of OM and stereology data, there was no correlation found between the process setting used and level of porosity. The hypothesis of the effects from hydrogen contamination and process settings could not be proved with the results from this data. In addition to aluminum vapor causing porosity, the aluminum content also plays a role in pore formation by altering the properties of liquid titanium. The theoretical model is used to build a physical understanding of the experimental results, which are discussed below.

To start, there was an unexpected relationship between the hydrogen content and the degree of porosity. It was found the wires with lower hydrogen content produced samples with less porosity than the samples deposited with higher hydrogen content wire. The level of contamination on the wire was expected to have the largest effect on porosity, so the hydrogen values that were used only represent the hydrogen contribution from the filler wire and not the baseplate or atmosphere as well. Since back streaming contamination is common, and given the long pump down times, there is expected to be a contribution of hydrogen from hydrocarbons in the atmosphere. An accurate relationship between the

hydrogen contamination from the wire and porosity cannot be established since there are other significant contributions of hydrogen to the system.

Next, CP-Ti was found to have more total porosity (spherical and faceted) and more faceted porosity compared to Ti-6Al-4V. Although, Ti-6Al-4V produced more spherical porosity than CP-Ti. These results can be explained using the theoretical model for pore formation and solubility of hydrogen in titanium. The main difference between the two sample sets is the addition of aluminum to titanium in Ti-6Al-4V. Alloying with aluminum alters the liquid properties of titanium that effect pore formation as well as the solubility of hydrogen in titanium. Adding aluminum decreases the surface tension and viscosity, causing Ti-6Al-4V to favor faster bubble nucleation and growth rates compared to CP-Ti. As a result, Ti-6Al-4V is expected to produce more pores that will grow to a larger size than CP-Ti. This is further supported by the plots of hydrogen solubility in Ti-6Al-4V and CP-Ti. Ti-6Al-4V has a lower solubility limit at the melting temperature meaning it will become supersaturated and reject hydrogen before CP-Ti. Also, CP-Ti solidifies at a single temperature compared to Ti-6Al-4V solidifying over a range of temperatures. This temperature range allows more time for hydrogen diffusion, bubble nucleation, and growth in Ti-6Al-4V. This is supported by the experimental results, where more spherical porosity was observed in Ti-6Al-4V.

It is more difficult to relate the theoretical model to the degree of faceted porosity, since the mechanism for forming a faceted pore is still not clear. The results from the X-ray CT analysis did not show any faceted pores, only spherical or LOF. Given this result and the morphology of the faceted pores, it is possible that they are formed as a result of removing an additional hydride or intermetallic

phase during grinding, although this phase is expected to be resolved in X-ray CT. Titanium

characteristically forms hydride phases when the hydrogen super-saturation limit is surpassed and not all

of the excess hydrogen is rejected. When aluminum is added to titanium, the HCP a and c lattice

parameters becomes strained, allowing solid titanium to hold more hydrogen. This increase in solid

solubility of hydrogen represses the ability to form a hydride phase since less hydrogen is available. This

means that Ti-6Al-4V suppressed hydride formation and will form less hydride phase compared to CP-Ti.

If it is assumed that the faceted pores are formed from the removal of a hydride or intermetallic, then this

supports the greater amount of faceted porosity observed in CP-Ti. With aluminum contents greater than

6 wt. %, Ti_3Al intermetallic phase may form. Under the same assumption as the hydride phase, it is

possible that this phase is removed from Ti-6Al-4V during grinding as well.

References

1. Frazier, W. E., et al. "Metal Additive Manufacturing: A Review." *Journal of Materials Engineering and Performance, Vol 23, ASM International,* 2014, 1917-1928.

2. R.N. Caron and J.T. Staley, Effects of Composition, Processing, and Structure on Properties of Nonferrous Alloys, *Materials Selection and Design, Vol 20, ASM Handbook, ASM International*, 1997, p 383-415

3. Schubert, G., Dr. "Electron Beam Welding - Process, Applicatons, and Equipment." *PTR-Precision Technologies Inc.* (n.d.): n. pag. Web.

4. ASTM Standard F2792–12a, 2016, "Standard Terminology for Additive Manufacturing Technologies," ASTM International, West Conshohocken, PA, 2003

5. Wille, G. W. and Davis, J. W. "Hydrogen in Titanium Alloys." *The U. S. Department of Energy* (1981) 8-22. Web.

6. Norrish, J., "Advanced Welding Process Technology and Process Control." Woodhead Publishing Limited, Abington Cambridge, England, 2006. Web.

7. Martin, A. S., and Manchester, F. D., "The H-Ti (Hydrogen-Titanium) System." *Buletin of Alloy Phase Diagrams, Vol 8.* No. 1 (1987) 30-42.

8. Welsch, G., Boyer, R., and Collings, E. W., editors. Materials Properties Handbook: Titanium Alloys. Ohio: ASM International, 1994. Web.

9. Møller, K.T., Progress in Natural Science: Materials International (2017)

10. Martukanitz, R. P. "Sources of Porosity in Gas Metal Arc Welding of Aluminum." (n.d.): n. pag. Web. Alcoa Labratories, Alcoa Center, Pa

11. Applied Research Lab. "Metallographic Analyses of Directed Electron Beam Depositions." (n.d.): n. pag. Web.

12. Huang, J. L. "On the mechanism of porosity formation during welding of titanium alloys." *Acta Materialia* 60.6-7 (2012): 3215-225. Web.

13. Adebayo, A., Mehnen J., and Tonnellier, X., "Effects of solid lubricants on wire and arc additive manufactured structures." *Proceedings of the Institution of Mechanical Engineers, Part B: Journal of Engineering Manufacture* 228.4 (2013): 563-71. Web.

14. Holinski, R., and J. Gänsheimer. "A study of the lubricating mechanism of molybdenum disulfide." *Wear* 19.3 (1972): 329-42. Web.

15. Kirchner, A., B. Klöden, J. Luft, T. Weißgärber, and B. Kieback. "Process window for electron beam melting of Ti-6Al-4V." *Powder Metallurgy* 58.4 (2015): 246-49. Web.

16. Juechter, V., T. Scharowsky, R.f. Singer, and C. Körner. "Processing window and evaporation phenomena for Ti–6Al–4V produced by selective electron beam melting." *Acta Materialia* 76 (2014): 252-58. Web.

17. Rettinghaus, G, and Huber, W.K., "Backstreaming in Diffusion Pump Systems." *6th International Vacuum Congress, Kyoto.* (1974). Web.

18. Maurice, L., Duval, P., and Gorinas, G., "Oil Backstreaming in Turbomolecular and Oil Diffusion Pumps." *J. Vac. Sci. Technol., 16(2),* Mar./Apr. (1979). Web.

19. Chen, Tao, Shengyong Pang, Qun Tang, Hongbo Suo, and Shuili Gong. "Evaporation Ripped Metallurgical Pore in Electron Beam Freeform Fabrication of Ti-6-Al-4-V." *Materials and Manufacturing Processes* 31.15 (2015): 1995-2000. Web.

20. Alcock, CB, Itkin, VP, and Horrigan MK Canadian Metallurgical Quartely 23, 309, (1984). Web

21. Mohandas, T., D. Banerjee, and V. V. Kutumba Rao. "Fusion zone microstructure and porosity in electron beam welds of an α β titanium alloy." *Metallurgical and Materials Transactions A* 30.3 (1999): 789-98. Web.

22. Harbe, Nikolas, and Timothy Quinn. "Effects of processing on microstructure and mechanical properties of a titanium alloy (Ti–6Al–4V) fabricated using electron beam melting (EBM), part 1: Distance from build plate and part size." *Materials Science and Engineering: A* 573 (2013): 264-70. Web.

23. Gegner, J. et al. "2D-3D Conversion of Object size Distributions in Quantitative Metallography." *Departments of Material Physics and Engineering.* D-97424 Schweinfurt Germany. Web.

24. Ganti, S. et al. "Comparison of Porosity Analysis Using 2D Stereology Estimated and 3D Serial Sectioning for Additively Manufactured Ti-6Al-2Sn-4Zr-2Mo Alloy." *Pract. Metallogr*. 54 (2017) 2. Web.

25. Exner, H.E. et al. "Stereology and 3D Microscopy: Useful Alternatives or Competitors in the Quantitative Analysis of Microstructures." *Image Anal. Stereol*. 23 (2004) 73-82. Web.

26. Lubetkin, S. D. "The Fundamentals of Bubble Evolution." Chemical Society Reviews (1995). 243-50. Web.

27. Zhou, K., Wang, H.P., Chang, J., and Wei, B., "Experimental Study of Surface Tension, Specific Heat, and Thermal Diffusivity of Liquid and Solid Titanium." *Chemical Physical Letters*. 639 (2015) 105-108. Web.

28. Zhou, K., Wei, B., "Determining Thermophysical Properties of Undercooled Liquid Ti-Al Alloy by Electromagnetic Levitation." *Chemical Physics Letters*. 521 (2012) 52-54. Web.

29. Egry, I., et al. "Thermophysical Properties of Liquid AlTi-Based Alloys" *International Journal of Thermophysics*. (2010). Web.

30. Kuznetsov, V. et al. "Aluminum-Hydrogen-Titanium Review." *Landolt-Bornstein MSIT*. (2004) 71-79

31. Su, Y. et al., "Hydrogen solubility in Molten TiAl Alloys." *International Hournal of Hydrogen Energy* 35 (2010) 8008-8013. Web.

32. Guang-Rui, J., Yan-Xiang, L., and YUAN, L., "Calculation of Hydrogen Solubility in Molten Metals." *Trans. Nonferrous Met. Soc.* 21(2011) 1130-1135. Web.

33. Lakomskii, V. I. "Change in the Solubility of Hydrogen in Metals at the Melting Point." *Izvestiya Rossiiskoi Akademii Nauk. Metally*. No. 2, pp. 187-190, (1992)

34. Talbot, D. E. J. and Anyalebechi, P. N., "Solubility of Hydrogen in Liquid Aluminum." *Materials Science and Technology Vol. 4* (1988).

Appendix

Raw Data from Wire Surface Chemistry Analysis

Raw XPS surface analysis data for Wire B

Wire B: Ti-6Al-4V								
XPS	F	O	Ti	N	Ca	C	S	Si	Al
at. %	1	29	7	2	<1	57	<1	2	1
Std. Dev.	± 0.4	± 1.3	± 0.9	± 0.5	± 0.1	± 1.6	± 0.1	± 0.2	± 0.3

Raw XPS surface analysis data for Wire C

Wire C: Ti-6Al-4V								
XPS	F	O	Ti	N	Ca	C	S	Si	Al
at. %	0	33	7	3	1	53	0	2	2
Std. Dev.	0	± 0.9	± 0.1	± 0.7	± 0.2	± 0.9	0	± 0.2	± 0.2

Raw XPS surface analysis data for Wire D

Wire D: CP-Ti								
XPS	Al	C	Ca	N	O	S	Si	Ti	V
at. %	0	86.3	2	0	9.9	0.3	1.3	0.4	0
Std. Dev.	0	± 0.6	± 0.2	0	± 0.4	± 0.2	± 0.3	± 0.3	0

Raw XPS surface analysis data for Wire E

Wire E: CP-Ti								
XPS	Al	C	Ca	N	O	S	Si	Ti	V
at. %	0	73.3	1.8	0	19.1	0.7	1.1	2.9	0
Std. Dev.	0	± 3.0	± 0.6	0	± 1.9	± 0.1	± 0.8	± 0.2	0

Raw Data from Optical Microscopy Porosity Evaluation

Raw data from Sample 1

Interface						Deposit						Average	
Size Class	A	B	C	D	E	Size Class	A	B	C	D	E	Interface	Deposit
0-49	1	2	2	5	2	0-49	35	8	12	24	12	2.4	18.2
50-99	1	0	4	3	0	50-99	3	3	3	8	2	1.6	3.8
100-149	0	0	3	0	2	100-149	2	0	2	1	0	1	1
150-199	0	0	2	0	0	150-199	1	0	1	1	0	0.4	0.6
200-249	0	0	0	0	0	200-249	0	0	1	0	2	0	0.6
250-299	0	0	1	0	0	250-299	0	1	0	0	1	0.2	0.4
300-349	0	2	0	0	0	300-349	1	0	0	0	0	0.4	0.2
350-399	0	1	0	0	0	350-399	1	0	0	0	1	0.2	0.4
>400	0	1	1	0	0	>400	3	1	0	0	0	0.4	0.8

Raw Data from Sample 2

Interface						Deposit						Average	
Size Class	A	B	C	D	E	Size Class	A	B	C	D	E	Interface	Deposit
0-49	3	3	2	7	11	0-49	25	7	12	50	55	5.2	29.8
50-99	1	4	1	4	5	50-99	2	9	3	11	21	3	9.2
100-149	0	3	0	2	1	100-149	2	3	2	3	4	1.2	2.8
150-199	0	0	0	0	0	150-199	0	4	1	4	0	0	1.8
200-249	1	0	0	0	0	200-249	1	2	1	1	0	0.2	1
250-299	0	0	0	0	0	250-299	0	3	0	1	1	0	1
300-349	0	0	0	0	0	300-349	1	2	0	0	0	0	0.6
350-399	0	0	0	0	0	350-399	0	0	0	0	0	0	0
>400	0	0	0	0	0	>400	1	1	0	0	0	0	0.4

Raw Data from Sample 3

Interface						Deposit						Average	
Size Class	A	B	C	D	E	Size Class	A	B	C	D	E	Interface	Deposit
0-49	1	5	0	4	5	0-49	25	21	9	6	16	3	15.4
50-99	0	1	0	3	2	50-99	11	18	0	6	0	1.2	7
100-149	2	0	0	0	0	100-149	1	7	0	4	4	0.4	3.2
150-199	1	0	0	0	0	150-199	0	0	0	1	0	0.2	0.2
200-249	1	0	0	0	0	200-249	1	0	0	0	0	0.2	0.2
250-299	0	0	0	0	0	250-299	0	0	0	0	0	0	0
300-349	0	0	0	0	0	300-349	1	0	0	0	0	0	0.2
350-399	0	0	0	0	0	350-399	0	0	0	0	0	0	0
>400	0	0	0	0	0	>400	0	0	0	0	0	0	0

Raw Data from Sample 4

Interface						Deposit						Average	
Size Class	A	B	C	D	E	Size Class	A	B	C	D	E	Interface	Deposit
0-49	9	0	0	0	0	0-49	34	3	1	6	4	1.8	9.6
50-99	1	0	1	0	2	50-99	11	4	4	2	2	0.8	4.6
100-149	1	0	0	0	0	100-149	2	2	2	0	3	0.2	1.8
150-199	0	0	0	0	0	150-199	1	0	2	0	0	0	0.6
200-249	0	0	0	0	0	200-249	1	0	1	1	0	0	0.6
250-299	0	0	0	0	0	250-299	0	0	0	0	0	0	0
300-349	0	0	0	0	0	300-349	0	0	0	0	0	0	0
350-399	0	0	0	0	0	350-399	0	0	0	0	0	0	0
>400	0	0	0	0	0	>400	8	0	0	0	0	0	1.6

Raw Data from Sample 5

Interface						Deposit						Average	
Size Class	A	B	C	D	E	Size Class	A	B	C	D	E	Interface	Deposit
0-49	3	0	0	2	8	0-49	14	1	0	16	16	2.6	9.4
50-99	0	0	2	2	4	50-99	2	1	3	4	6	1.6	3.2
100-149	0	0	0	2	1	100-149	1	2	0	1	1	0.6	1
150-199	0	0	0	0	0	150-199	2	1	0	0	0	0	0.6
200-249	0	0	0	0	0	200-249	0	0	0	1	0	0	0.2
250-299	0	0	0	0	0	250-299	0	0	1	0	0	0	0.2
300-349	0	0	0	0	0	300-349	0	0	0	0	0	0	0
350-399	0	0	0	0	0	350-399	0	0	0	0	0	0	0
>400	0	0	0	0	0	>400	1	1	0	1	2	0	1

Raw Data from Sample 6

Interface						Deposit						Average	
Size Class	A	B	C	D	E	Size Class	A	B	C	D	E	Interface	Deposit
0-49	2	2	3	0	4	0-49	31	8	2	4	19	2.2	12.8
50-99	4	1	3	0	0	50-99	15	6	1	1	5	1.6	5.6
100-149	1	0	0	0	0	100-149	3	5	1	1	2	0.2	2.4
150-199	0	0	0	0	0	150-199	4	5	0	0	0	0	1.8
200-249	0	0	0	0	0	200-249	0	1	0	0	0	0	0.2
250-299	0	0	0	0	0	250-299	0	0	0	0	0	0	0
300-349	0	0	0	0	0	300-349	0	0	0	0	0	0	0
350-399	0	0	0	0	0	350-399	0	1	0	0	0	0	0.2
>400	0	0	0	0	0	>400	3	0	0	0	1	0	0.8

Raw Data from Sample 7

Interface						Deposit						Average	
Size Class	A	B	C	D	E	Size Class	A	B	C	D	E	Interface	Deposit
0-49	1	0	1	1	13	0-49	61	7	1	15	41	3.2	25
50-99	1	2	0	0	1	50-99	15	2	3	9	14	0.8	8.6
100-149	0	0	0	0	0	100-149	1	2	2	4	1	0	2
150-199	2	0	0	1	0	150-199	1	0	3	4	2	0.6	2
200-249	0	0	0	0	0	200-249	0	0	0	0	0	0	0
250-299	0	0	0	0	0	250-299	0	0	0	1	0	0	0.2
300-349	0	0	0	0	0	300-349	0	0	0	0	0	0	0
350-399	0	0	0	0	0	350-399	0	0	0	0	0	0	0
>400	0	0	0	0	0	>400	0	0	0	1	0	0	0.2

Raw Data for Sample 8

Interface						Deposit						Average	
Size Class	A	B	C	D	E	Size Class	A	B	C	D	E	Interface	Deposit
0-49	4	0	0	1	4	0-49	22	3	12	11	13	1.8	12.2
50-99	2	0	1	0	1	50-99	14	7	7	0	9	0.8	7.4
100-149	0	0	1	0	0	100-149	8	3	7	0	0	0.2	3.6
150-199	0	0	0	0	0	150-199	3	1	3	0	0	0	1.4
200-249	0	1	0	0	0	200-249	0	1	1	0	0	0.2	0.4
250-299	0	1	0	0	0	250-299	0	0	0	0	0	0.2	0
300-349	0	0	0	0	0	300-349	0	0	0	0	0	0	0
350-399	0	0	0	0	0	350-399	0	0	0	0	1	0	0.2
>400	0	0	0	0	0	>400	0	0	0	0	0	0	0

Raw Data for Sample 9

Interface						Deposit						Average	
Size Class	A	B	C	D	E	Size Class	A	B	C	D	E	Interface	Deposit
0-49	3	13	7	2	3	0-49	35	35	11	29	8	5.6	23.6
50-99	1	3	5	5	0	50-99	12	8	14	4	1	2.8	7.8
100-149	0	0	0	1	0	100-149	11	1	5	1	1	0.2	3.8
150-199	1	0	0	1	0	150-199	2	1	2	1	0	0.4	1.2
200-249	0	0	0	1	0	200-249	2	0	2	1	0	0.2	1
250-299	0	0	0	0	0	250-299	0	0	2	0	0	0	0.4
300-349	0	0	1	0	0	300-349	0	1	1	0	0	0.2	0.4
350-399	0	0	0	0	0	350-399	0	0	0	0	0	0	0
>400	0	0	1	0	0	>400	0	0	0	1	0	0.2	0.2

Raw Data for Sample 10

Interface						Deposit						Average	
Size Class	A	B	C	D	E	Size Class	A	B	C	D	E	Interface	Deposit
0-49	1	3	0	9	3	0-49	63	16	3	28	15	3.2	25
50-99	0	2	0	0	1	50-99	40	5	2	8	7	0.6	12.4
100-149	0	0	0	1	0	100-149	22	8	1	4	2	0.2	7.4
150-199	0	0	0	0	0	150-199	6	0	0	2	2	0	2
200-249	0	0	0	0	0	200-249	0	4	0	0	1	0	1
250-299	0	0	0	0	0	250-299	0	0	0	0	0	0	0
300-349	0	0	0	0	0	300-349	0	5	0	0	0	0	1
350-399	0	0	0	0	0	350-399	0	0	0	0	0	0	0
>400	0	0	0	0	0	>400	0	1	0	0	0	0	0.2

Raw Data for Sample 11

Interface						Deposit						Average	
Size Class	A	B	C	D	E	Size Class	A	B	C	D	E	Interface	Deposit
0-49	8	7	0	7	6	0-49	63	13	15	28	8	5.6	25.4
50-99	3	5	1	4	2	50-99	16	9	7	5	5	3	8.4
100-149	0	2	0	2	0	100-149	4	8	7	4	4	0.8	5.4
150-199	0	1	1	0	0	150-199	3	7	5	0	2	0.4	3.4
200-249	0	0	2	0	0	200-249	0	4	4	0	1	0.4	1.8
250-299	0	0	0	0	0	250-299	0	0	1	0	0	0	0.2
300-349	0	0	0	0	0	300-349	0	4	1	0	0	0	1
350-399	0	0	0	0	0	350-399	0	2	0	0	0	0	0.4
>400	0	0	0	0	0	>400	2	3	1	0	0	0	1.2

Raw Data for Sample 12

Interface						Deposit						Average	
Size Class	A	B	C	D	E	Size Class	A	B	C	D	E	Interface	Deposit
0-49	5	8	2	1	2	0-49	28	18	14	5	33	3.6	19.6
50-99	2	3	1	0	3	50-99	9	18	3	6	13	1.8	9.8
100-149	1	1	1	1	0	100-149	6	10	0	2	4	0.8	4.4
150-199	0	0	0	0	0	150-199	0	6	2	0	6	0	2.8
200-249	0	2	0	0	0	200-249	0	1	3	0	0	0.4	0.8
250-299	0	0	0	0	0	250-299	0	3	2	0	1	0	1.2
300-349	0	1	0	0	0	300-349	0	2	0	0	0	0.2	0.4
350-399	0	0	0	0	0	350-399	0	1	0	0	1	0	0.4
>400	0	0	0	0	0	>400	0	5	1	0	0	0	1.2